UNIVERSITY OF HELSINKI REPORT SERIES IN PHYSICS

Physics D286

# Physics of positrons and defect excitations in solids: a Quantum Monte Carlo study

**Kristoffer Simula**

Helsinki Institute of Physics
Helsinki Accelerator Laboratory
Division of Materials Physics
Department of Physics
Faculty of Science
University of Helsinki
Helsinki, Finland

DOCTORAL DISSERTATION

*to be presented for public discussion with the permission of the Faculty of Science of the University of Helsinki, in Porthania, PIII K00201-119, Yliopistonkatu 3, Helsinki, on 29th of September, 2023 at 13 o'clock.*

HELSINKI 2023

ISBN 978-951-51-9436-7 (printed version)
ISSN 0356-0961
Helsinki 2023

Kristoffer Simula, **Solid-state physics of positrons and defect excitations with Quantum Monte Carlo**, University of Helsinki, 2023, University of Helsinki Report Series in Physics, (printed version)

# Abstract

In contemporary physics, computer simulations often bridge the gap between theory and experiments. This is thanks to algorithmic and hardware developments in recent decades, as well as the need for a large number of floating-point calculations when studying the quantum mechanical properties of atomic matter. In this work, we use quantum mechanics-based algorithms to study positron annihilation in solids and the optical properties of the nitrogen-vacancy center in diamond.

Positrons have important applications in science, including studies of fundamental laws of physics, medical imaging, and atomic matter spectroscopy. Positron annihilation spectroscopy is particularly useful for studying solid-state matter and its defects, but requires accurate theory to support the measurements.

Previous state-of-the-art theories supporting positron annihilation spectroscopy of solids have been based on density functional methods, which treat the particles in a system as independent and only approximate interparticle correlations with correlation functionals.

In this work, we present a quantum Monte Carlo method for simulating positrons in solids. The method was developed by the author through the implementation of new features into an existing simulation package. It does not include free parameters in simulations, like density functional theories, and explicitly includes correlations. By comparing the calculated positron lifetimes and momentum densities of annihilating electron-positron pairs in well-known pristine solids to experiment, we show that our method is superior to previous theories in supporting positron-based spectroscopy.

The final part of this work examines the ability of quantum Monte Carlo to capture strong correlations of a solid-state defect, the nitrogen-vacancy center in diamond, which is of wide interest in material science due to its potential use in quantum technology applications. By calculating the vertical excitation energies of the defect and comparing them to other quantum chemistry methods, we demonstrate that our method can simulate large simulation cells without relying on embedding schemes, making it a promising method for further studies of solid-state qubits.

The success of our studies on positrons in pristine solids and the nitrogen-vacancy center in diamond shows that quantum Monte Carlo can be widely applied to systems of interest, such as vacancy defects in crystalline solids, in positron-based material science. This work lays the groundwork for an improved practical theory of positrons in solids.

# Tiivistelmä

Laskennallinen fysiikka auttaa ymmärtämään teorian ja kokeellisen tutkimuksen välistä yhteyttä. Viime vuosikymmenten nopea algoritmien ja tietokoneiden kehitys ja atomirakenteiden kvanttimekaaniseen kuvaukseen vaadittava laskuoperaatioiden suuri lukumäärä asettavat laskennallisen tutkimuksen keskeiseen rooliin nykyfysiikassa. Tässä työssä kvanttimekaniikkaan perustuvia algoritmeja käytetään kiteisissä aineissa tapahtuvan positroniannihilaation ja timantin typpivakanssikeskuksen optisten ominaisuuksien tutkimiseen.

Positroneja voidaan käyttää fysiikan perusteiden tutkimuksessa, lääketieteellisessä kuvantamisessa sekä materiaalitutkimuksessa. Positroniannihilaatiospektroskopia on erityisen hyödyllinen kiinteän aineen ja sen kidevirheiden tutkimuksessa, mutta mittaustulosten ymmärtämiseen tarvitaan tarkkoja teoreettisia menetelmiä.

Tähän mennessä parhaat teoreettiset positroniannihilaation tutkimusmenetelmät ovat perustuneet tiheysfunktionaaliteoriaan, joka käsittelee materiaaleja itsenäisistä hiukkasista koostuvina kokonaisuuksina. Kvanttimekaniikan ennustamat hiukkasten väliset keskinäiset riippuvuudet, korrelaatiot, sisällytetään tiheysfunktionaaliteoriassa korrelaatiofunktionaaleihin, jotka perustuvat osin arvauksiin vuorovaikutusten luonteesta.

Tässä työssä kehitettiin kvantti Monte Carlo -menetelmä positronien simulointiin kiinteissä aineissa. Työn aikana ohjelmoitiin uusia ominaisuuksia olemassa olevaan laajempaan laskutyökaluun. Kvantti Monte Carlo kuvaa korrelaatiot hyvin määritellyllä teorialla. Laskemalla positronien elinaikoja ja annihiloituvien elektroni-positroniparien liikemäärätiheyksiä tunnetuissa virheettömissä kiteissä ja vertaamalla tuloksia kokeiden kanssa osoitetaan uusi menetelmä tarkemmaksi ja ennusteiltaan luotettavammaksi kuin tiheysfunktionaaliteoriaan pohjautuvat menetelmät.

Työn viimeinen osa tutkii kvantti Monte Carlo-menetelmän kykyä kuvata vahvoja korrelaatioita timantin kidevirheessä, typpi-vakanssikeskuksessa. Tämä systeemi on materiaalitieteissä laajan kiinnostuksen kohteena sen lupaavien kvanttiteknologian sovellusten vuoksi. Laskemalla virheen vertikaalisia viritysenergioita ja vertaamalla tuloksia muiden kvanttikemian menetelmien sekä kokeellisten tutkimusten tuloksiin näytetään, kuinka uusi lähestymistapa pystyy mallintamaan korrelaatiot sisällyttäen enemmän hiukkasia kidevirheen mallinnukseen kuin mihin aiemmat teoriat ovat kyenneet. Laskennan ei siksi tarvitse tukeutua kvanttiupotusmalleihin. Työssä esitetään kvantti Monte Carlo-menetelmää lupaavaksi uudeksi työkaluksi kiinteän aineen kubittien tutkimuksessa.

Työn positroni- ja kidevirhetutkimusten onnistuneet laskutulokset osoittavat kehitettyjen laskentamenetelmien laaja-alaisen soveltamisen positronispektroskopioiden kannalta kiinnostavien systeemien, kuten vakanssien, kannalta mahdolliseksi. Näin ollen työ antaa vahvan pohjan paremmalle käytännön teorialle positronien tutkimiseen kiinteässä aineessa.

# Contents


Abstract . . . . . v
Tiivistelmä . . . . . vi
Contents . . . . . vii
Summaries of publications . . . . . x
Common abbreviations . . . . . xi

**1 Introduction** **1**
1.1 Quantum Monte Carlo and simulation of materials . . . . . 1
1.2 Simulation of positron annihilation . . . . . 3
1.3 Optical properties of the nitrogen-vacancy center in diamond . . . 5

**2 Theory** **8**
2.1 Schrödinger equation . . . . . 8
2.2 Independent particles do not exist . . . . . 9
2.2.1 Non-interacting Hamiltonian . . . . . 10
2.2.2 Slater determinant . . . . . 10
2.2.3 Exchange interaction . . . . . 11
2.2.4 Particle correlation and pair correlation function . . . . . 11
2.2.5 Treatment of correlations in mean-field theories . . . . . 12
2.3 Many-body wave function . . . . . 13
2.3.1 Full solution . . . . . 13
2.3.2 Slater-Jastrow wave function . . . . . 14
2.3.3 Cusp conditions . . . . . 15
2.3.4 Spin in Slater-Jastrow wave function . . . . . 16
2.3.5 Backflow function . . . . . 17
2.4 Periodic solids, Bloch orbitals and periodic wave functions . . . . . 18

2.4.1 Finite-size errors . . . . . 19
2.5 Pseudopotentials . . . . . 20

**3 Computational methods** **22**
3.1 Variational Monte Carlo . . . . . 22
3.1.1 Estimation of observables . . . . . 22
3.1.2 Optimization of the wavefunction . . . . . 23
3.2 Diffusion Monte Carlo . . . . . 23
3.2.1 Basic principles . . . . . 23
3.2.2 Fixed-node approximation . . . . . 24
3.2.3 Importance sampling . . . . . 25
3.3 Basis sets . . . . . 26
3.4 Vibrational effects . . . . . 27

**4 Studies of positrons in solids** **30**
4.1 Overview . . . . . 30
4.2 QMC with positrons . . . . . 30
4.2.1 Hamiltonian . . . . . 30
4.2.2 Wave function . . . . . 31
4.2.3 Positron-nucleus interactions . . . . . 32
4.2.4 Nodal surface and fixed-node error . . . . . 32
4.3 Positron Annihilation . . . . . 33
4.3.1 Annihilator operator . . . . . 33
4.3.2 Positron lifetime . . . . . 35
4.3.3 Analysis of the pair correlation function data . . . . . 37
4.3.4 Annihilating-pair momentum density . . . . . 39
4.4 Results . . . . . 41
4.4.1 Lifetime results from quantum Monte Carlo simulations . . 41
4.4.2 Effect of atomic vibrations on positron lifetimes in Si . . . . 43
4.4.3 Doppler broadening of the annihilation radiation . . . . . 43

**5 Vertical excitation energies of the $NV^-$-center in diamond 46**

5.1 Overview . . . . . 46

5.2 Modeling the electronic states . . . . . 49

5.2.1 Constructing the wave functions for the $NV^-$-center . . . . 49

5.2.2 Variational principle for excitation energies with diffusion Monte Carlo . . . . . 52

5.2.3 Nodal surface errors . . . . . 53

5.2.4 Spin contamination . . . . . 53

5.2.5 Finite-size errors . . . . . 54

5.3 Results . . . . . 55

**6 Summary 56**

Acknowledgements . . . . . 60

References . . . . . 62

# Summaries of publications

**Publication I: Quantum Monte Carlo simulation of positron lifetimes in solids**

Simula, K.A., Muff, J.E., Makkonen, I., and Drummond, N.D., Phys. Rev. Lett. **129**, 166403 (2022)

In this Publication, a new computational tool based on quantum Monte Carlo was introduced for the simulation of positrons in solids. The method is validated by estimating the positron lifetimes in C, AlN, Si, and Li and comparing against experiments.

The author was responsible for the development of the simulation tool for positrons, performing the lifetime calculations, developing and running algorithms for vibrational studies of positrons, and writing the article.

**Publication II: Quantum Monte Carlo study of Doppler broadening of positron annihilation radiation in semiconductors and insulators**

Simula, K.A., Härkönen, J., Zhelezova, I., Drummond, N.D., Tuomisto, F., and Makkonen, I., Phys. Rev. B **108**, 045201 (2023)

The simulation of positrons in solids was continued in this Publication with a focus on prediction of the Doppler broadening of the annihilation spectra in solids. The predictions required further developments to the quantum Monte Carlo method. Comparisons of the estimated Doppler spectra with experiment were used to prove the usability of the method.

The author developed most of the methods to predict Doppler spectra. The author also performed the calculations for the Doppler spectra, and did the comparisons against experiment. The article was written in collaboration with I. Makkonen and the author.

**Publication III: Calculation of the energies of the multideterminant states of the nitrogen vacancy center in diamond with quantum Monte Carlo**

Simula, K.A. and Makkonen, I., *Accepted for publication in Phys. Rev. B in August 2023*

In this Publication it was studied how quantum Monte Carlo could be utilized in calculation of the excitation energies of the negatively charged nitrogen-vacancy center in diamond. The final results reach essential features of the excitation spectrum, showing the ability of diffusion Monte Carlo to describe electronic structure with strong static correlations.

The author was responsible for defining and planning the research problem, the calculations, theoretical considerations, and testing of the quantum Monte Carlo for the problem. The author also wrote the article.

# Common abbreviations

**QMC** Quantum Monte Carlo

**VMC** Variational Monte Carlo

**DMC** Diffusion Monte Carlo

**HF** Hartree-Fock

**DFT** Density functional theory

**PCF** Pair correlation function

**APMD** Annihilating-pair momentum density

**NV** Nitrogen-vacancy (center)

# Chapter 1

# Introduction

## 1.1 Quantum Monte Carlo and simulation of materials

Quantum physics, when applied to the study of electronic structure of materials, poses a well-defined theoretical problem: how to investigate the properties of a given condensed matter system, given that the nature of the electronic interactions are exactly known? The logical answer is that the properties can be known when the totality of interactions is used in calculation of the quantum states of the system. However, this totality is often much too complicated for exact calculations [1]. Exact quantum states become computationally intractable already with systems beyond simple molecules or a dozen or so electrons, leaving us able to study properties of only the smallest atoms and molecules exactly.

There are several reasons for the cost of computations. The interactions of electrons are Coulombic, and can be treated pairwise so that the total description of the system interactions includes the sum over all of the electronic pairs. Therefore, the complexity of the description increases factorially with the number of electrons $N$, i.e. the system size. In a $D$-dimensional system the total dimensionality of the wave function is $ND$, and this increases computational challenges. Also, when considering large systems the size of the wave function can be impractically large to be treated with current computer architectures.

Because the exact description of large systems is out of reach for any group of people with any current or future classical computer resources, approximations are needed. A good approximation allows one to ignore certain aspects of the system, or interactions, so that the computational efficiency is improved, while the accuracy of the computations is kept sufficient for solving practical quantum mechanical problems. The value of an approximation is in combination of its predictive power and computational efficiency.

A reasonably general guideline for sufficient accuracy can be based on energy considerations. At room temperature, the usual energy scale relevant for quantum phenomena in atomic matter is $\sim 25$ meV/electron. Chemical accuracy, largely thought as the sufficient accuracy for theoretical treatment of quantum mechanical systems, is defined to be below the threshold of 1 kJ/Mol, or 43meV/electron. However, the energy scale of 1 Ha/atom, with the Hartree energy of 27.2 eV, is a natural energy scale for the Schrödinger equation of atomic matter. In materials consisting of larger atoms the relevant energy scale can be much larger. This means that an accurate method used to describe materials in quantum level should be able to reach an accuracy of at least five significant digits in calculating energy of a system. In terms of computational efficiency, an approximate method is in general hoped to have polynomial scaling with system size, with the possibility of extrapolating the results to infinite system sizes in studies of periodic materials. A generally applicable method satisfying the requirements of chemical accuracy and polynomial scaling is not currently available. Today in computational quantum mechanics new methods are constantly being developed and old ones are being improved, with accuracy and computational efficiency being gradually pushed beyond current limits. However, many systems of interest to both theory and applications are still too complicated for us to treat with chemical accuracy because of computational limitations.

The correlation of interacting particles is of central interest in quantum physics. The correlation arises from the repulsive effect of same-spin particles due to the Pauli exclusion principle, and from the Coulomb interactions. The energy decrease of a system due to correlation effects can be only a small fraction of the total energy, but for many systems and properties of interest, such as those studied in this thesis, the correlations are central.

The most widely used approximation in treating the quantum problem of materials is to treat the electrons as independent particles. This means that the correlation between the particles is not explicitly included in the treatment. The interaction between the electrons is included in the description of a given system by a mean-field potential. Methods that incorporate this approximation include Hartree-Fock (HF) and density functional theory (DFT) [2–4]. These methods are very useful, as they are computationally inexpensive and often reach high accuracy. However, they do not reach the chemical accuracy consistently and may fail qualitatively in treating systems and properties dependent on strong correlations. DFT, that approximates the correlations by utilizing exchange-correlation functionals drafted with only a guess of the properties of the real systems, can offer multiple ways to treat a given problem, often having significant spread between the results provided by the different options, as also shown in Publications I-II of this thesis.

Quantum Monte Carlo (QMC) methods are among the most accurate electronic structure methods. They can treat the electronic interactions and correlations explicitly by using stochastic sampling of the wave function. Stochasticity al-

lows one to focus on only the most relevant parts of the Hilbert space where the wave function of a given system has the largest amplitudes. This accelerates the computations required for accurate description of electronic systems significantly. Simple QMC methods include variational Monte Carlo [5], that utilizes the Metropolis algorithm [6] to stochastically sample the square of an electronic wave function. This method is entirely dependent on the form of the wave function ansatz [5]. More accurate methods include projector Monte Carlo methods such as diffusion Monte Carlo (DMC) [5, 7] and auxiliary-field Monte Carlo [8, 9], which can often reach chemical accuracy for small systems [5, 10]. However, in projector methods the antisymmetry of electronic wave functions leads to the infamous fermion sign problem, where the sampling of the negative and positive regions of the wave functions leads to exponential growth of the statistical error and therefore of the simulation time. The sign problem is believed to be NP-hard, severely limiting the available solutions [11]. In DMC, this problem is circumvented with the fixed-node approximation, with the expense of introducing fixed-node error into the simulation. Another QMC method, full configuration interaction QMC [12], treats the wave function exactly without approximations, but is despite the speedup provided by stochastic sampling a very expensive method computationally, and is applied mostly to small system sizes.

Chapters 2 and 3 in this Thesis present the basic theory in wave function based modelling of solids and the use of VMC and DMC in application of the theory. Then, it is presented how VMC and DMC methods, working with wave functions constructed with HF and DFT, are used to study problems relevant for contemporary science and engineering. One of these problems is the description of positron annihilation in metals, semiconductors and insulators (Publications I and II in this thesis). Another is the prediction of optical properties of point defects in solid-state matter, with special focus on the NV center in diamond (Publication III).

## 1.2 Simulation of positron annihilation

Positron annihilation is a process of quantum electrodynamics, where an electron and a positron annihilate at collision, releasing two (in the more likely case of opposite-spin electron-positron pair) photons with the energy of 511 keV according to Einstein's mass-to-energy principle [13, 14]. The process has utility in fundamental physics [15], medicine [16], and material science [17–24]. In solid-state materials, the utility of positron annihilation spectroscopies lies especially in the study of open-volume defects [14]. When positron is injected into a sample, it first thermalizes rapidly, and then it settles into a delocalized state in bulk materials or, in case of encountering open-volume defects, the positron can easily localize and trap within these defects. Eventually the positron will annihilate. In non-defected solid state materials, the positron usually collides with an electron and annihilates after a time interval of $100 - 450$ picoseconds. If the positron

settles into a trapped state at a vacancy, its average overlap with the electrons gets smaller and the lifetime increases. The annihilation photons can be detected. Accumulating spectra of these photons enables measurement of positron lifetime or the Doppler broadening of the annihilation radiation [14].

The positron lifetime is a measure of the total electron-positron overlap, and the Doppler broadening reveals information on the momentum density of annihilating pairs and depends on the momentum distribution of the electrons and the positron. The lifetime and momentum measurements can distinguish the types and amounts of open-volume defects in a sample [14]. The measurements can be combined with e.g. *in situ* irradiation experiments [23] or optical illumination of the sample [24], enabling study of further system properties. Lifetime studies of thin films and lifetime scanning of surfaces are possible with pulsed positron beams [17, 20]. Also Fermi surfaces of metals can be studied [22]. Overall positron annihilation spectroscopy is a valuable tool for material science and semiconductor industry.

Theoretical understanding of the electronic states of the sample material and the injected positron is necessary to relate the measured spectra to the microstructures of the sample. As quantum mechanical treatment of solid-state matter requires model systems of $20 - 1000$ electrons, the wave functions cannot be found exactly. Instead, efficient and accurate computational methods must be used.

A computational method for the calculation of the electronic and positronic states must be able to model the correlations between the particles. Until the methods presented in Publication I-II of this thesis, extensions to DFT-based methods have been the state-of-the-art in the field of positron simulations in solids, generally referred to as two-component density functional theory (TCDFT) [25–31]. There are also more sophisticated methods based on Green's function methods and perturbation theory for studies of positrons attached to molecules that have demonstrated excellent accuracy against experiments [32].

With TCDFT one usually simulates single positron in an electronic system, where electron-positron correlations are incorporated in functionals of local densities, although semilocal and nonlocal functionals are also used in studies of positron states at surfaces or vacancy clusters [33–35].

The calculation of positron lifetime is done with TCDFT by estimating the total overlap of electrons and positrons with another functional of densities, the enhancement factor, which is the value of the electron-positron pair correlation function at zero distance [14]. The enhancement factor is not known exactly in TCDFT calculations, but is instead constructed either by higher-level methods for simple model systems, such as in Ref. [36], or by fitting to experimental data, as in Ref. [31]. The annihilating-pair momentum density (APMD) has been computed with TCDFT by relying on the enhancement factor in the so-called state-independent model. In state-dependent model, the APMD is computed by

using state-specific enhancement factors [14]. Neither the state-dependent or -independent model is exact in the definition of APMD, even in the exact DFT formulation.

The application of TCDFT for simulation of positrons in solids has been fairly successful, but the method suffers from the usual problems of DFT-based modelling. The correlations play a significant part in the positron annihilation process, and hence a simulation model should be able to describe the relevant interactions. TCDFT does not have an electron-positron correlation functional that could be generally applied to different systems of interest; certain functional can provide accurate results in some system while failing in others. An example is given in Publication I, where lifetime calculations are performed in different bulk materials with a set of enhancement factors that provide lifetimes with a spread of even 30 ps in the same material. Furthermore, we cannot know *a priori* which functional should be chosen for a given simulation problem. Same kind of problems are related to estimation of the APMD; Publication II shows how state-dependent and -independent models can provide impractically large differences in the Doppler spectra of the annihilation radiation.

During the course of the work presented in this thesis a QMC method for the simulation of positrons in solids was developed. The method can be generally applied to bulk insulators, semiconductors and metals and defects within them, as well as to surfaces and interfaces. It includes the exact Coulomb interaction between the particles in the simulations and treats the correlations explicitly. Using QMC, positron lifetimes were calculated in diamond, Si, AlN and Li in Publication I. Also the APMD was calculated in Publication II in all of these materials except the metallic Li. The required sizes of the simulated systems as well as the sufficient levels of wave function complexities were studied. The convergent results were compared against experimental lifetime data and Doppler spectra, showing unprecedented accuracy. Importantly, the effect of lattice vibrations on the annihilation parameters, so far unknown in theoretical simulations, was also studied and found to be insignificant in Si.

The improved results over previous theory in This thesis show how explicitly correlated methods should be used to overcome the usual issues present in positron simulations with TCDFT. Hence the methods presented in this Thesis significantly improve the applicability of positron-based spectroscopies.

## 1.3 Optical properties of the nitrogen-vacancy center in diamond

The final part of this thesis consists of studies of the optical excitation spectra of the nitrogen-vacancy (NV) center in diamond. This system is among the first point-like solid-state defect discovered to have potential applications in quantum technology. Qubits built out of solid-state defects, or spin defects, have non-zero

ground state spin and suitable excited state structure. They can have long coherence times [37, 38], manipulation of their ground-state spin is possible even at room temperature [39, 40], and the ground-state spin can be initialized with optical pumping [41]. The ground-state spin state of solid-state qubits can be read optically or electronically [42, 43]. The coupling of the ground state-spin with the nearby nuclear spins enables very promising routes in improving the operation and applicability of the solid-state qubits [37, 39, 44–46]. Due to its early discovery, the NV center has been both theoretically and experimentally the most widely studied spin qubit, and its vertical excitation spectrum is very accurately determined. This makes this system an ideal testbed for new theoretical approaches aiming at capturing the properties of solid-state defects. Hence, before simulating positrons in solid-state defects, the ability of quantum Monte Carlo to capture strong correlations in these systems is tested by calculating the excitation energies.

However, the study on the NV center presented in this thesis is not done solely for the purposes of positron studies. Correlated studies of lattice defects with respect to magneto-optical properties is a fairly new field of study in theoretical condensed matter physics [47] with numerous methods proposed to tackle the problem [48–52]. The use of quantum Monte Carlo for the optical properties of the NV center in diamond presents a new approach. A variant of quantum Monte Carlo, the diffusion Monte Carlo method [5], has been previously used to study solid-state defect migration and formation energies [53–56], and even few results exist for optical excitations [53, 57, 58]. Another variant, full configuration interaction Monte Carlo, was recently used to study the multireference nature of the states in the NV center [59]. However, the previous quantum Monte Carlo methods have not been used to study solid-state defects with system sizes found to be convergent with respect to the excitation energies of the NV center. Also the use of a powerful correction scheme for capturing the electronic correlations, the backflow correction, has not been used previously for solid-state defects. In the work of this thesis, the results on the vertical excitation energies of the NV center are computed in simulation cell sizes up to 216 atoms and extrapolated to infinite system size, and are further corrected with backflow.

The results for the excitation energies of the NV center presented in this thesis in both the preface and in Publication III are found to be competitive with other state-of-the-art many-body simulation methods. The excitation energies are overestimations, but certain features and optical transitions are captured very accurately. Because of the power of quantum Monte Carlo to simulate large system sizes, and because the variational nature of the wave functions used by the method, there is plenty of scope to apply quantum Monte Carlo for studies of immediate interest in the development of qubits based on solid-state defects. Furthermore, the successful simulation of the excitations also demonstrate the methods ability to capture strong correlations related to solid-state defects, paving the way for simulation of positrons trapped at the open volumes within

solids.

# Chapter 2

# Theory

In this chapter, the main theoretical concepts, approximations and tools relevant for the application of quantum Monte Carlo methods for the physical phenomena studied in this thesis are presented. First, the Schrödinger equation is presented. Then, the HF and DFT theories are quickly presented along with their treatment of many-body correlations. The main body of this chapter is in discussing the many-body theory of quantum mechanics relevant for QMC methods. Finally, the application of theory in periodic systems and the pseudopotential approximations used to treat the atomic cores are covered.

## 2.1 Schrödinger equation

We can analyse the properties of a system of interest in condensed matter theory by forming the time-independent Schrödinger equation,

$$\hat{H}\Psi = E\Psi, \tag{2.1}$$

that completely describes the system. The formulation starts by constructing a Hamiltonian operator $\hat{H}$. $\hat{H}$ operates on a – initially unknown – wavefunction $\Psi$ and gives the energy of the system. The solution of the Schrödinger equation gives all the states $\Psi_n$ with energy $E_n$. The state with lowest energy, the ground state, is the most important for describing static properties of any given system.

The total energy consists of the interaction and kinetic energies of the particles. Because the mass ratio between electron and a nuclei $m_e/M$ is between $10^{-3}$ and $10^{-5}$ for any given atom, we can assume that the kinetic energy of nuclei is very small compared to the kinetic energy of electrons. This allows us, without losing accuracy, to treat the properties of the electrons with frozen nuclear coordinates, by only including the electron-nucleus Coulomb interactions and no nuclear kinetic energy into the Hamiltonian. This simplification is called

the Born-Oppenheimer approximation, leading to the following Hamiltonian for systems consisting of electrons:

$$\hat{H} = -\frac{1}{2}\sum_i \nabla^2_{\mathbf{r}_i} - \sum_I \sum_i \frac{Z_I}{|\mathbf{r}_i - \mathbf{r}_I|} + \frac{1}{2}\sum_i \sum_{j\neq i} \frac{1}{|\mathbf{r}_i - \mathbf{r}_j|}. \tag{2.2}$$

Above, $\mathbf{r}_i$ are the coordinates of electron $i$, where $i = 1, ..., N$ and $N$ the number of electrons in the system. The first term in $\hat{H}$ is a sum over kinetic energies of the individual electrons. The second accounts for the electron-nucleus interaction energies, where the nuclear charge and position of nucleus $I$ are denoted as $Z_I$ and $\mathbf{r}_I$, respectively. The last term in $\hat{H}$ includes the electron-electron Coulomb interactions. It should be noted that we are not including spin dependence in the Hamiltonian. In the work presented in this dissertation, the properties studied are not spin-dependent, and hence we are not considering the spin-orbit interaction in the simulations.

The wavefunction $\Psi$ can be solved from the Schrödinger equation when we know the Hamiltonian, but for fermions (such as electrons and positrons) we must impose an additional constraint for $\Psi$, which states that interchange of two particles in the system amounts to reversing the sign of the wavefunction. This means that $\Psi$ must be antisymmetric according to the Pauli exclusion principle.

In general, we are not able to solve $\Psi$ exactly except for systems with only a few electrons. The Schrödinger equation for electrons is known to be NP-hard [11], meaning that the computational complexity scales exponentially with the number of electrons in the system. To define a model system that realistically represents crystalline materials, we need to consider from dozens up to thousands of electrons. In the next sections, the methods are shown used in this work to simplify the solution of the Scrödinger equation without losing the accuracy to the extent of losing the predictive power of the simulations. The notation $x_i = (\mathbf{r}_i, \sigma_i)$ is used to denote the spatial and spin degrees of freedom for electron $i$ in a given system.

## 2.2 Independent particles do not exist

Correlations between particles are present in any many-body system, and their effect is crucial in understanding the phenomena studied in this work. Even the mean-field methods such as the HF theory that ignores the correlations but includes the exchange effects, or DFT that uses correlation functionals to approximately describe exchange and correlation effects, include some amount of correlations to the simulations. Below, theory behind methods treating non-interacting particles is shortly presented and the correlations are discussed.

### 2.2.1 Non-interacting Hamiltonian

A widely applied simplification in the treatment of electronic systems is to ignore the electron-electron interaction term of the Hamiltonian, and instead describe the electron interactions via an effective potential $V_{\text{eff}}$ containing the electron interactions with the nuclei and other electrons. The non-interacting Hamiltonian $\hat{H}_0$ of an $N$-electron system can be written as

$$\hat{H}_0 = -\frac{1}{2}\sum_i \nabla^2_{\mathbf{r}_i} + \sum_i V_{\text{eff}}(x_i) = \sum_i \hat{H}^i_0. \tag{2.3}$$

Solutions to the Schrödinger equation with this kind of simplified Hamiltonian give wave functions with electronic states describing electrons that behave independently of other electrons. Methods treating electrons as independent particles are often called singe-particle methods.

In this work we have used two single-particle methods, the Hartree-Fock (HF) method and Kohn-Sham DFT, to obtain the single-particle states as building blocks for a many-body wavefunction ansatz used in QMC simulations.

### 2.2.2 Slater determinant

Within the single-particle picture, the wavefunction $\Psi$ is in principle separable as

$$\Psi(x_1, x_2, ..., x_N) = \phi_1(x_1)\phi_2(x_2)...\phi_N(x_N) \tag{2.4}$$

and the solution of the Schrödinger equation of the non-interacting system is obtained by solving the single-particle states $\phi$ as

$$\hat{H}^i_0\phi_i(x_i) = \epsilon_i\phi_i(x_i). \tag{2.5}$$

We can construct an antisymmetric wavefunction that obeys the Pauli principle out of the solutions of the form in Eq. (2.4) as Slater determinants:

$$\Psi(x_1, x_2, ..., x_N) = D(x_1, x_2, ..., x_N) = \frac{1}{\sqrt{N!}}\begin{vmatrix} \phi_1(x_1) & \phi_1(x_2) & ... & \phi_1(x_N) \\ \phi_2(x_1) & \phi_2(x_2) & ... & \phi_2(x_N) \\ ... & & & \\ \phi_N(x_1) & \phi_N(x_2) & ... & \phi_N(x_N) \end{vmatrix} \tag{2.6}$$

The Slater determinants impose the Pauli principle correctly; in case two rows contain the same state, $D$ is zero, and if two particles of same spin are overlapping, having the same spatial coordinates, $D$ is also zero. Also the exchange of rows or columns in the Slater determinant results change of sign, hence satisfying the Pauli principle. Based on the properties of $D$, we can also assume orthonormality of single-particle states.

### 2.2.3 Exchange interaction

We can use the Slater determinant as in Eq. (2.6) as a guess for the many-body wavefunction $\Psi$. The expectation of the many-body Hamiltonian $\hat{H} = \hat{H}_0 + \hat{H}_I$ (Eq. (2.2)), with $\hat{H}_I$ including the Coulomb electron-electron interaction, is then

$$\begin{aligned}\langle D|\hat{H}|D\rangle &= \langle D|\hat{H}_0 + \hat{H}_I|D\rangle \\ &= \sum_i \langle\phi_i|\hat{H}_0^i|\phi_i\rangle \\ &+ \frac{1}{2}\sum_i\sum_{j\neq i}\Big[\langle\phi_i\phi_j|\hat{H}_I|\phi_i\phi_j\rangle - \langle\phi_i\phi_j|\hat{H}_I|\phi_j\phi_i\rangle\Big]\end{aligned} \tag{2.7}$$

with

$$\begin{aligned}\langle\phi_i|\hat{H}_0^i|\phi_i\rangle &= \int \phi_i(x)\hat{H}_0\phi_i(x)dx \\ \langle\phi_i\phi_j|\hat{H}_I|\phi_k\phi_l\rangle &= \int\int \phi_i(x)\phi_j(x')\frac{1}{|\mathbf{r}-\mathbf{r}'|}\phi_k(x)\phi_l(x')dxdx'\end{aligned} \tag{2.8}$$

The above equations introduce the braket notation as an alternative way to denote quantum mechanical wave functions and the operators acting on them. The notation is used in similar fashion in this thesis from now on.

In Eq. (2.7), the first term after the second equality represents the sum over single-particle energies. The second term represents the electron self-interaction, often called the Hartree interaction, and the third term the exchange interaction.

The exchange interaction is present due to the Pauli exclusion principle. It is repulsive for same-spin electrons and nonexistent for the electron pairs of antiparallel spins. Its effect is to always lower the energy by keeping the electrons of same spin apart.

The Hartree-Fock (HF) method [60, 61] uses a single Slater determinant as a wave function ansatz, and is based on finding the determinant with lowest energy, as calculated in Eq. (2.7). The HF method can give good predictions for various properties of atoms, molecules and bulk matter. However, the wave functions given by HF do not include correlations beyond exchange, and for example in the case of positron lifetime calculations HF method overestimates the experimental lifetimes, even by an order of magnitude in some cases.

### 2.2.4 Particle correlation and pair correlation function

When the wave function is approximated to be a Slater determinant, the particle exchange interactions introduce correlation between the particles in a system. However, the correlations present in the wave function are not limited to exchange effects. Solution of the Schrödinger equation with the full Hamiltonian and no restrictions on the form of the wave function, when possible, gives dramatically more complicated wavefunctions than just a single Slater determinant. In

electronic systems this is because the repulsive interaction between the electrons introduce particle correlations beyond the exchange effects.

A usual interpretation of the exchange-correlation effects between particles of equal charge in some materials is that the repulsive interactions create a volume of decreased charge density around the particles. This volume is often called the exchange-correlation hole, and hence the particles with the holes surrounding them can be reinterpreted as quasiparticles of a point charge and a surrounding cloud of opposite charge, with both the point charge and the charge of the cloud having the same magnitude [4].

The energies due to correlation effects are often only a small percentage of the total energy of a given system [5]. However, some system properties can greatly depend on the exchange and other correlations. As shown in this thesis, the inclusion of correlation effects is crucial in predicting positron annihilation parameters and optical transitions in the NV center.

Because the interactions in any quantum mechanical system are pairwise, we can examine the correlations in the system with pair correlation functions. The joint probability of finding electrons $i$ and $j$ with spins $\sigma_i$ and $\sigma_j$ at points $\mathbf{r}_i$ and $\mathbf{r}_j$ (presented as diagonal elements of the pair density matrix in Sec. 4.3.2) is [4]

$$\begin{aligned} n(\mathbf{r}_i,\sigma_i;\mathbf{r}_j,\sigma_j) &= \left\langle \Psi \left| \sum_{i\neq j} \delta(\mathbf{r}-\mathbf{r}_i)\delta(\sigma-\sigma_i)\delta(\mathbf{r}'-\mathbf{r}_j)\delta(\sigma'-\sigma_j) \right| \Psi \right\rangle \\ &= N(N-1)\sum_{\sigma_3,\sigma_4...}\int |\Psi(\mathbf{r},\sigma,\mathbf{r}',\sigma',\mathbf{r}_3,\sigma_3,...,\mathbf{r}_N,\sigma_N)|^2\, d\mathbf{r}_3,...,\mathbf{r}_N. \end{aligned} \tag{2.9}$$

The above formula assumes that $\Psi$ is normalized to unity. When there is no correlation between particles $i$ and $j$, the joint probability is just the product of the individual particles probabilities. Hence we can measure the amount of correlation as $\Delta n(\mathbf{r}_i,\sigma_i;\mathbf{r}_j,\sigma_j) = n(\mathbf{r}_i,\sigma_i;\mathbf{r}_j,\sigma_j) - n(\mathbf{r}_i,\sigma_i)n(\mathbf{r}_j,\sigma_j)$, giving us a way to rewrite the joint probability:

$$n(\mathbf{r}_i,\sigma_i;\mathbf{r}_j,\sigma_j) = n(\mathbf{r}_i,\sigma_i)n(\mathbf{r}_j,\sigma_j) + \Delta n(\mathbf{r}_i,\sigma_i;\mathbf{r}_j,\sigma_j). \tag{2.10}$$

With Eq. (2.10), we can define the pair correlation function (PCF) as

$$g(\mathbf{r}_i,\sigma_i;\mathbf{r}_j,\sigma_j) = \frac{n(\mathbf{r}_i,\sigma_i;\mathbf{r}_j,\sigma_j)}{n(\mathbf{r}_i,\sigma_i)n(\mathbf{r}_j,\sigma_j)} = 1 + \frac{\Delta n(\mathbf{r}_i,\sigma_i;\mathbf{r}_j,\sigma_j)}{n(\mathbf{r}_i,\sigma_i)n(\mathbf{r}_j,\sigma_j)}. \tag{2.11}$$

The PCF is a measure of correlation between particles. At long distances, the PCF approaches the value of one, $lim_{|\mathbf{r}_i-\mathbf{r}_j|\to\infty} g(\mathbf{r}_i,\sigma_i;\mathbf{r}_j,\sigma_j) = 1$. At short and intermediate distances the PCF deviates from one. We will see that PCF plays a crucial role in estimating positron lifetimes in bulk matter.

### 2.2.5 Treatment of correlations in mean-field theories

As mentioned above,the HF method can find the Slater determinant with lowest energy, and describe therefore a many-body system with exchange interactions

included. However, the correlations beyond exchange are out of reach for the method. Density functional theory (DFT) is a method that attempts to capture the exchange-correlation effects with correlation functionals of particle density.

In DFT the system energy is defined as a functional of charge density. DFT can be used to find the single-particle states that minimize the energy functional. The effective potential $V_{\text{eff}}$ (see Eq. (2.3)), included in the DFT energy functional, is made to include a correlation functional component that approximately tries to capture the effect of correlations to the energy and other properties. Correlation functionals for DFT can be constructed by, e.g. doing exact calculations for correlations in homogenous electron gas

In hybrid DFT, the exchange functional is typically expressed as a linear combination of the exact exchange of the HF theory and a DFT exchange functional. Hybrid DFT can be more accurate in describing quantum mechanical systems, but is also more expensive because of the calculation of the HF exchange.

In this work, HF, DFT, and hybrid DFT are used to solve the single-particle states for construction of Slater determinants. Depending on the system studied, the quality of the resulting wavefunction may not be strongly dependent on the choice of the single-particle method. Only in the case of the optical transitions in the NV center we see improvement in the predictive power of the calculations if hybrid DFT orbitals are used. The next section described how the wavefunctions are defined to include correlations beyond exchange into the wavefunction consisting of one or multiple Slater determinants.

## 2.3 Many-body wave function

The computational methods used in this work include the Coulomb interactions explicitly in the Hamiltonian and the treatment of the many-body correlations in the simulation. The methods simulate systems with the wave function generally not exactly known. However, the Hamiltonian is known exactly. Here full solution to the many-body Schrödinger equation and the wave functions used in this work are presented. Also, important theoretical concepts relevant for simulating the wave functions, such as cusp conditions, the backflow function and the treatment of spins in the wave functions are presented.

### 2.3.1 Full solution

The single-particle orbitals solved with Hamiltonian $\hat{H}_0^i$ as in Eq. (2.3) can be used in constructing Slater determinants. Slater determinants can then be used as a basis for the eigenstates of the full Hamiltonian $\hat{H}$, and we can define the many-body wavefunction as

$$\Psi(x_1, x_2, ..., x_N) = \sum_{\mathbf{i}} C_{\mathbf{i}} D_{\mathbf{i}}(x_1, x_2, ..., x_N), \tag{2.12}$$

where $\mathbf{i}$ represents the indexing of orbitals as they appear in the Slater determinant: with $\mathbf{i} = (i_1, i_2, ..., i_N)$, the orbitals in $D_\mathbf{i}$ appear as the orthogonal set $\phi_{i_1}, \phi_{i_2}, ..., \phi_{i_N}$. Because the determinant is antisymmetric under interchange of any two orbitals, we can restrict the indices $\mathbf{i}$ to $i_1 < i_2 < ... < i_N$.

Full solution of the Schrödinger equation would have to include all of the possible determinants of the system. Many numerical methods, such as full configuration interaction methods, take $M > N$ single-particle orbitals (from e.g. HF or DFT), define all the possible Slater determinants $D_\mathbf{i}$ obtainable by populating $N$ electrons into the $M$ orbitals, and solve the array of coefficients $C_\mathbf{i}$ that minimizes the energy with full Hamiltonian $\hat{H}$ and wavefunction $\Psi$ as in Eq. (2.12). The solution of the coefficients giving minimum energy boils down to an eigenvalue problem. The number of orbitals $M$ and electrons $N$ used in the simulation can be increased up to convergence, but this is very expensive in practice for all but very small systems. In small systems where this is possible, other, approximative many-body methods can be benchmarked against the full solution by e.g., comparing the amount of energy retrieved by the approximate method compared to the full solution.

### 2.3.2 Slater-Jastrow wave function

Instead of solving the full many-body wave function as a sum of all the possible Slater determinants in the system, we can use an approximative wave function ansatz capable of including beyond-exchange correlation effects, and solve it for minimum energy. With a good ansatz, the solution of the Schrödinger equation is not too costly and the obtained wave function can give sufficiently accurate predictions on the properties of interest in a given system. The ansatz used in this work has the form of the so called Slater-Jastrow wavefunction [62]:

$$\Psi(x_1, x_2, ..., x_N) = e^{J(x_1, x_2, ..., x_N)} \sum_n^{N_d} C_n D_n(x_1, x_2, ..., x_N), \tag{2.13}$$

where the sum is over a finite number $N_d$ of determinants, chosen by a case-dependent consideration. Often only one determinant is included, as the correlations are often described sufficiently by the Jastrow factor $J$ [63–65], or by projector methods such as DMC. However, in some cases multiple determinants are needed. For example, the symmetries of the system might require the wave function to be determined by multiple determinants, as seen with the states of the NV center. Also the Jastrow factor (and the backflow function, see below) may not describe some correlations sufficiently, in which case additional determinants may improve the description of the system.

The Jastrow factor mainly used in this work can be written as [66]

$$J(x_1, x_2, ..., x_N) = \sum_{i=1}^{N-1} \sum_{j=i+1}^{N} u_{P_{ij}}(r_{ij}) + \sum_{I=1}^{N_{ions}} \sum_{i=1}^{N} \chi_{S_{iI}}(r_{iI}) + \sum_{I=1}^{N_{ions}} \sum_{i=1}^{N-1} \sum_{j=i+1}^{N} f_{T_{ijI}}(r_{iI}, r_{jI}, r_{ij}). \tag{2.14}$$

Above, $N_{ions}$ is the number of nuclei in a given system, $r_{ij} = |\mathbf{r}_i - \mathbf{r}_j|$ and $r_{iI} = |\mathbf{r}_i - \mathbf{r}_I|$. The $u$, $\chi$, and $f$ terms of the Jastrow factor are isotropic, parametrized functions describing interparticle correlations. The $u$-term describes particle-particle, $\chi$-term particle-ion, and the $f$-term particle-particle-ion correlations. In other words, the $f$-term describes particle-particle correlations conditioned on the particle distance from closeby ions. The symbols $P$, $S$, and $T$ index the terms of the Jastrow factor according to different particle groupings, so that different terms can be used for pairs of electrons with parallel or antiparallel spins, or for electron-positron pairs, and also for different nuclei [7].

The $u$-term gives the homogenous particle-pair correlations and gives the most significant improvement to the wave function out of the terms in the Jastrow factor. $u$-term includes the effect of repulsive electron-electron correlations to the wave function, tending to homogenize the electronic cloud, resulting also to too large electronic amplitudes close to the nuclei. The $\chi$-term, giving the effect of correlation interactions between the electrons and the nuclei, can correct the effect by the $u$-term. The $f$-term gives further inhomogenous correlation corrections. In positron annihilation studies, the $u$-term gives the most important contribution to the electron-positron correlations at contact.

### 2.3.3 Cusp conditions

In the full Hamiltonian in Eq. (2.2) we can see that the Coulomb terms diverge when two particles – electrons, positrons or nuclei – are coalescent. In a perfectly realistic wavefunction the kinetic energy should diverge also so that it cancels the Coulomb divergence. However, in approximative wave functions this cancellation is not ensured. Hence the cancellation must be imposed in the approximate wave function to satisfy the cusp conditions [67, 68].

We use pseudopotentials (see Sec. 2.5), where the potential energy is finite at the electron- or positron-nucleus cusp. Hence the electron-nucleus cusp conditions are satisfied. To inspect the cusp conditions for overlapping electrons and/or positron (with particle indices $i$ and $j$), we define their charges to be $q_i$ and $q_j$, the reduced mass to be $\mu_{ij}$ and the separation $r = |\mathbf{r}_i - \mathbf{r}_j|$. Then the local energy is finite at $r \to 0$ when the wave function $\Psi$ satisfies

$$\left( \frac{1}{\Psi} \frac{\partial \Psi}{\partial r} \right)_{r \to 0} = \frac{2 q_i q_j \mu_{ij}}{d \pm 1} = \Gamma_{ij}, \tag{2.15}$$

where $d$ is the dimension of the system and the plus and minus signs correspond to $i$ and $j$ being distinguishable and indistinguishable particles, respectively. In our calculations the cusps are imposed into the $u$-term of the Jastrow factor so that $\partial u/\partial r_{ij} = \Gamma_{ij}$ [7].

### 2.3.4 Spin in Slater-Jastrow wave function

So far the wave functions have been considered with inherent dependence on the particle spins. However, in general the wave functions used in this work are spin-independent. The quantum mechanical observables studied in this work are spin-independent (excluding the fact that we are mostly concerned with annihilations between electron-positron pairs of antiparallel spin, but this can be ignored here), making the use of these wave functions justified.

Consider the particle coordinates $x_i = (\mathbf{r}_i, \sigma_i)$. We can define a spin function

$$\zeta_1(\sigma_1, \sigma_2, ..., \sigma_N) = \xi_\uparrow(\sigma_1)\xi_\uparrow(\sigma_2), ..., \xi_\uparrow(\sigma_{N_\uparrow})\xi_\downarrow(\sigma_{N^\uparrow+1})\xi_\downarrow(\sigma_{N^\uparrow+2}), ..., \xi_\downarrow(\sigma_N), \tag{2.16}$$

where $N_\uparrow$ ($N_\downarrow$) denotes the number of up-(down-)spin electrons. The $N!/N_\uparrow!N_\downarrow$ index permutations of $\zeta_1$ form an orthonormal set, allowing us to expand a wave function $\Psi$ as

$$\Psi(x_1, x_2, ..., x_N) = \sum_i F_i(\mathbf{r}_1, \mathbf{r}_2, ...\mathbf{r}_N)\zeta_i(\sigma_1, \sigma_2, ..., \sigma_N) \tag{2.17}$$

If $\Psi$ is antisymmetric we know that $F_i$ are antisymmetric under like-spin exchange of particles. Besides that, all $F_i$ are the same instead of the indexing. Because of the orthonormality of $\zeta_i$, for spin-independent operators [such as the Hamiltonian in Eq. (2.2)] the expectation value over $\Psi$ [see Eq. (3.1)] is the same as over $F_1$. Hence we can use $F_1$ instead of $\Psi$ as our spin-independent wave function. In the case the wave function is represented as a sum of Slater determinants, $\Psi = \sum_n c_n D_n$, we have [69]

$$F_1(\mathbf{r}_1, \mathbf{r}_2, ...\mathbf{r}_N) = \sum_n c_n D_n^\uparrow(\mathbf{r}_1, \mathbf{r}_2, ...\mathbf{r}_{N_\uparrow}) D_n^\downarrow(\mathbf{r}_{N_\uparrow+1}, \mathbf{r}_{N_\uparrow+2}, ...\mathbf{r}_N) \tag{2.18}$$

The Slater-Jastrow wave function $\Psi^{SJ}$ [as in Eq. (2.13)] can be decomposed similarly as in Eq. (2.17), and by using only the $F_1$ for estimation of spin-independent observables we can write our spin-independent Slater-Jastrow wave function as [69]

$$\Psi^{SJ}(\mathbf{r}_1, \mathbf{r}_2, ...\mathbf{r}_N) = e^{J(\mathbf{r}_1, \mathbf{r}_2, ...\mathbf{r}_N)} \sum_n c_n D_n^\uparrow(\mathbf{r}_1, \mathbf{r}_2, ...\mathbf{r}_{N_\uparrow}) D_n^\downarrow(\mathbf{r}_{N_\uparrow+1}, \mathbf{r}_{N_\uparrow+2}, ...\mathbf{r}_N) \tag{2.19}$$

which is the form used in the studies of this work.

In general, the wavefunction of a system should be an eigenfunction of the total spin of the particles, $S^2$, and the spin-$z$ projection of the total spin, $S_z$. Because

in the wave function in Eq. (2.19) there is a discrete amount of spin-up and -down electrons, it is an eigenfunction of $S_z$, but not of $S^2$. With certain combinations of spin-dependent determinants as in Eq. 2.13 the wave function can be an eigenstate of $S^2$ with a spin-independent Jastrow factor. However, if the different cusps for parallel and antiparallel spin pairs are imposed in the Jastrow the spin symmetry breaks again. The error of the wavefunction due to incorrect spin symmetries is called spin contamination [69].

### 2.3.5 Backflow function

The Slater-Jastrow wave function is constructed out of single-particle orbitals, that are in this work obtained from HF or Kohn-Sham DFT simulations. Hence the Slater determinant is only approximately representing the system. The Jastrow factor can retrieve most of the correlations. However, when greater precision is needed, we further improve the description of correlations in this work by including a backflow correction [70, 71] in the wave function.

Feynman and Cohen introduced the idea of the backflow correction already in 1956 [72] to capture excitation energies in liquid helium. In a backflow wave function the particle coordinates appearing in the Slater determinant are replaced by quasiparticle coordinates,

$$\mathbf{r}_i^q = \mathbf{r}_i + \zeta_i(\mathbf{R}), \tag{2.20}$$

where $\mathbf{R} = (\mathbf{r}_1, ..., \mathbf{r}_N)$ and

$$\begin{aligned}\zeta_i(\mathbf{R}) = &\sum_{j\neq i}^{N} \eta_{P_{ij}}(r_{ij})\mathbf{r}_{ij} + \sum_{I}^{N_I} \mu_{S_{iI}}(r_{iI})\mathbf{r}_{iI} \\ &+ \sum_{j\neq i}^{N}\sum_{I}^{N_I} \left[\psi_{T_{ijI}}(r_{ij}, r_{iI}, r_{jI})\mathbf{r}_{ij} + \Theta_{T_{ijI}}(r_{ij}, r_{iI}, r_{jI})\mathbf{r}_{ij}\right]\end{aligned} \tag{2.21}$$

and $N_I$ is the number of nuclei in the system [7]. The backflow function consists of one-, two-, and three-body terms $\eta$, $\mu$, and $\phi$, with the particle groupings $P$, $S$, and $T$ just as for the Jastrow factor in Eq. (2.14). Hence the coordinates of particle $i$ are dependent on the coordinates of all the other particles in the system. $\zeta_i$ can be determined variationally and is supposed to describe the flow pattern of a quantum fluid, where particles are adapting to the movement of a single particle by moving away from its path and filling the void left behind the particle.

## 2.4 Periodic solids, Bloch orbitals and periodic wave functions

As the studies of quantum mechanical properties are limited in terms of the computing power, we need to approximate the large-scale systems, such as solids studied in this work, with smaller model systems. Defect-free solids can to a good approximation be estimated as infinite periodic crystals. In this work these crystals are studied within simulation cells with periodic boundary conditions, so that the properties of the cells represent properties of the infinite crystals.

The single-particle states of a periodic atomic lattice must transform as Bloch functions under the action of spatial translations over lattice vectors of the primitive cell of the lattice. The invariance of the Hamiltonian in Eq. (2.3) under periodic boundary conditions can be imposed by making $V_{\text{eff}}$ periodic. The resulting periodic single-particle Schrödinger equation is obeyed by the Bloch orbitals

$$\phi_{\mathbf{k}}(\mathbf{r}) = u_{\mathbf{k}}(\mathbf{r})e^{i\mathbf{k}\cdot\mathbf{r}}, \tag{2.22}$$

where $\mathbf{r}$ contains the coordinates of a particle occupying the orbital, and $\mathbf{k}$ is a 3-dimensional vector of the reciprocal space. $u_{\mathbf{k}}(\mathbf{r})$ is a function satisfying the periodicity and $e^{i\mathbf{k}\cdot\mathbf{r}}$ is a plane-wave.

To impose periodic boundary conditions on the many-body Hamiltonian of a simulation cell, we must require it to fulfill the following conditions [73]

$$\hat{H}((\mathbf{r}_1, ..., T_{\mathbf{N}}\mathbf{r}_i, ...\mathbf{r}_N)) = \hat{H}(\mathbf{r}_1, \mathbf{r}_2, ...\mathbf{r}_N) \tag{2.23}$$

$$\hat{H}((T_{\mathbf{n}}\mathbf{r}_1, ..., T_{\mathbf{n}}\mathbf{r}_i, ..., T_{\mathbf{n}}\mathbf{r}_N)) = \hat{H}(\mathbf{r}_1, \mathbf{r}_2, ...\mathbf{r}_N), \tag{2.24}$$

where $T_{\mathbf{n}}, \mathbf{n} = (n_1, n_2, n_3)$ represents a translation over linear combination of primitive cell lattice vectors $\mathbf{a}_i, i \in (1, 2, 3)$, and $T_{\mathbf{N}}, \mathbf{N} = (N_1, N_2, N_3)$ is the translation operator in the simulation cell lattice vector basis.

Condition (2.23) stems from the use of finite simulation cell, or supercell, in the calculation. Condition (2.24) defines the electron symmetry under simultaneous translation of all the electrons by a lattice vector of the primitive cell of the crystal. Introducing the many-body Bloch states

$$\Psi_{\mathbf{k}_s}(\mathbf{r}_1, \mathbf{r}_2, ...\mathbf{r}_N) = U_{\mathbf{k}_s}(\mathbf{r}_1, \mathbf{r}_2, ...\mathbf{r}_N)e^{i\mathbf{k}_s\cdot\sum_{i=1}^{N}\mathbf{r}_i} \tag{2.25}$$

$$\Psi_{\mathbf{k}_p}(\mathbf{r}_1, \mathbf{r}_2, ...\mathbf{r}_N) = W_{\mathbf{k}_p}(\mathbf{r}_1, \mathbf{r}_2, ...\mathbf{r}_N)e^{i\mathbf{k}_p\cdot\frac{1}{N}\sum_{i=1}^{N}\mathbf{r}_i} \tag{2.26}$$

we can state that (2.25) stems from (2.23) and (2.26) from (2.24) [63, 64]. $\mathbf{k}_p$ and $\mathbf{k}_s$ can be restricted within the first Brillouin zone of the primitive and simulation cells, respectively. $U$ has the periodicity of the simulation cell for every electron and $W$ is invariant under application of $T_{\mathbf{n}}$ to all electrons simultaneously.

When solving the electron states with a single-particle method, it is common to define a grid of reciprocal lattice vectors $\mathbf{k}_p$ in which to solve the orbitals of the

form $u_{\mathbf{k}_p}(\mathbf{r})e^{i\mathbf{k}_p\cdot\mathbf{r}}$ in a simulation cell. If the simulation cell is the primitive cell, an uniform $\mathbf{k}_p$-vector grid within the reciprocal primitive cell of size $N_1 \times N_2 \times N_3$ along the primitive reciprocal lattice vectors can be used to define a set of orbitals, and in principle the density of the grid can be increased up to convergence in computations to increase the momentum resolution of the single-particle method.

With single-particle states in the primitive cell and with the $N_1 \times N_2 \times N_3$ $\mathbf{k}_p$-vector grid, a supercell consisting of $N_1 \times N_2 \times N_3$ primitive cells along the primitive lattice vector directions can be defined so that the $\mathbf{k}_p$-vectors of the single-particle orbitals all fold to the $k_s$ (usually the $\Gamma$-point). Hence the single-particle orbitals for construction of a many-body wave function in a larger simulation cell can be solved within a smaller simulation cell, such as the primitive cell, with multiple $\mathbf{k}_p$ vectors.

If the center of the $\mathbf{k}_p$-vector grid is not zero but $\mathbf{k}_s$, the phase of the many-body wave function is $\mathbf{k}_s$ as in Eq. (2.25). A sensible choice of $\mathbf{k}_s$ can reduce finite-size effects (see next section).

### 2.4.1 Finite-size errors

The use of periodically repeated finite simulation cells introduce numerous errors in the simulation, that can be defined as $\delta(N) = E_\infty - E_N$, where $N$ is the number of particles in the simulation cell.

To correctly model the properties that are evaluated in momentum space, we would need to integrate over a continuum of momentum vectors, but in finite-size simulation cells we need to evaluate the integrals in a discrete momentum grid. This introduces a bias to the simulation. The errors due to discrete momentum grid decrease as the size of the simulation cell is increased, as the momentum grid densifies. Instead of increasing the simulation cell size, one can decrease these errors by using a technique called twist averaging [74]. In this scheme system properties are evaluated as averages over a set of wavefunctions having different phase $\mathbf{k}_s$ (see previous section), where $\mathbf{k}_s$ set the origin for the momentum grids. Also by running only a single simulation with a well-chosen $\mathbf{k}_s$ can improve the results.

Other finite-size errors in many-body simulations include the interaction of the exchange-correlation hole with its periodic images. We also have errors in the simulation if the size of the simulation cell is not large enough to include long-range interactions of the particles correctly.

Further errors arise from forcing the Friedel oscillations of the pair density to be commensurate with the simulation cell. These errors are quasirandom in nature and cannot be fully removed from the simulations.

Also in case of charged simulation cells, as with neutral systems with positron included, or with the negatively charged NV center, we have an error originating from the periodic repetition of the finite net charge, resulting in infinite charge for

the simulated system. This charge is compensated by introducing a homogenous jellium charge into the simulation cell.

Another source of finite-size error present in the simulation of the NV center is the periodic repetition of the defect in the simulated lattice. If too small simulation cell is used, the defect can interact with its periodic images, leading to errors in the description of the system.

The single-particle finite-size errors can be studied with single-particle methods to find whether the many-body simulation is done in a convergent cell size. There also exists numerous correction schemes to estimate $\delta(N)$ for individual sources of errors [73]. One expensive but reliable method is to use extrapolation formulas. Defining

$$E_\infty = E_N + F(N), \tag{2.27}$$

we can compute system energy in a set of simulation cells with different particle numbers $N$, and extrapolate to infinite system size. The use of extrapolation formulas requires knowledge of the form of the function $F$. In Publication III, we use an extrapolation formula of the above form with linear dependence of $F$ on $1/N$, which should apply when the excitation is local in its nature, to obtain the vertical excitation energies in infinite system size. The calculations are done for simulation cells with 254- and 866-electrons.

The most simple way of studying the finite-size errors is to increase the simulation cell until convergence in results is found. This can often be expensive.

## 2.5 Pseudopotentials

The widely applied approximation in quantum mechanical treatment of atomic matter is to use pseudopotentials to represent the atomic nuclei and the core electrons. Core electrons are bound to individual nuclei and do not participate in atomic bonding. The pseudopotentials include the core electrons within the so called frozen core approximation, and introduce a potential for the valence electrons caused by the atomic nuclei and the surrounding core electrons.

The pseudopotentials work when the nuclear degrees of freedom can be ignored, i.e., within Born-Oppenheimer approximation, and when we are concerned with observables mainly determined by the valence electrons. It is good practice to use different pseudopotentials to ensure the properties under study are invariant under the change of pseudpotentials. In the positron studies of this work we have used both Dirack-Fock (DF) average relativistic pseudopotentials [75, 76] and effective core potentials (ECP) [77], and we have done an all-electron calculation for Li to see whether position lifetime is affected by the full inclusion of the core electrons within the simulation [5]. In general, the pseudopotential approximation in positron simulations is valid when $d$-shell electrons are not included in the frozen core. If a material consists of atoms with $d$-shell electrons, the availability

of such pseudopotentials can restrict the capability of effectively simulating the material, as including the $d$-electrons to the frozen core can provide wrong results, while treating the $d$-electrons explicitly can be too expensive.

# Chapter 3

# Computational methods

The results for the positron annihilation parameters in different materials as well as for the vertical excitation energies in the NV center in diamond are obtained by using the VMC and DMC methods. DMC is the more accurate of the two, in fact it is one of the most accurate methods available to date for studies of systems consisting of up to 2000 electrons [7]. However, VMC is always used first for optimizing the variational wave function used for importance sampling in the DMC simulation. The form of the VMC wave function also defines the nodal surface, that determines the accuracy of the DMC simulations. The basic principles of these two methods are presented here, as well as the theory and algorithms used to renormalize positron annihilation parameters with respect to lattice vibrations.

## 3.1 Variational Monte Carlo

### 3.1.1 Estimation of observables

We can write the wave function of a system of $N$ particles as $\Psi(\mathbf{R})$, where $\mathbf{R} = (\mathbf{r}_1, ..., \mathbf{r}_N)$ contains the spatial coordinates of the particles in the system and is called a configuration or a walker. We can estimate the expectation value of a quantum mechanical local or semilocal (spin-independent) operator $\hat{O}(\mathbf{R})$ as

$$\langle \Psi \left| \hat{O}(\mathbf{R}) \right| \Psi \rangle = \frac{\int d\mathbf{R} \Psi(\mathbf{R}) \hat{O}(\mathbf{R}) \Psi^*(\mathbf{R})}{\int d\mathbf{R} \left| \Psi(\mathbf{R}) \right|^2} \tag{3.1}$$

Calculating the expectation value in a 3-dimensional system requires the calculation of a $3N$-dimensional integral. To use Monte Carlo integration to estimate the expectation value, we can define a local operator as

$$\hat{O}_{loc}(\mathbf{R}) = \frac{\hat{O}(\mathbf{R})\Psi(\mathbf{R})}{\Psi(\mathbf{R})} \tag{3.2}$$

so that

$$\langle \hat{O} \rangle = \frac{\int d\mathbf{R} \left|\Psi(\mathbf{R})\right|^2 \hat{O}_{loc}(\mathbf{R})}{\int d\mathbf{R} \left|\Psi(\mathbf{R})\right|^2} \approx \quad \frac{1}{M} \sum_{m=1}^{M} \hat{O}_{loc}(\mathbf{R}_m), \tag{3.3}$$

where the set $\{\mathbf{R}_m\}, m = 1, ..., M$, sampled from $\left|\Psi(\mathbf{R})\right|^2$ can be obtained with the Metropolis algorithm [6].

### 3.1.2 Optimization of the wavefunction

The way the Schrödinger equation is approximately solved within the variational Monte Carlo scheme is through wave function optimization. We choose a parametrized wave function form $\Psi_\alpha(\mathbf{R})$, such as the Slater-Jastrow wave function where the parameters are included in the Jastrow factor, and estimate its energy according to Eq. (3.3). The variational principle states that, in the limit $M \to \infty$, the energy $E_\alpha^{VMC}$ obtained is always greater or equal than the true ground-state energy $E_0$ of the system, and the variance of the energy $\mathrm{Var}_\alpha^{\mathrm{VMC}}$ is always greater or equal to zero:

$$E_\alpha^{\mathrm{VMC}} = \frac{1}{M} \sum_{m=1}^{M} E_{loc}(\mathbf{R}_m) \geq E_0 \tag{3.4}$$

$$\mathrm{Var}_\alpha^{\mathrm{VMC}}(\mathbf{R}) = \frac{1}{M} \sum_{m=1}^{M} \left[E_{\mathrm{loc}}(\mathbf{R}_m) - E_\alpha^{\mathrm{VMC}}\right]^2 \geq 0 \tag{3.5}$$

where $E_{loc}(\mathbf{R}) = \Psi_\alpha^{-1}(\mathbf{R})\hat{H}\Psi_\alpha(\mathbf{R})$. Hence the energy in the variational Monte Carlo scheme is a function of the parameters in the trial wave function.

The parameters can be optimized by either minimizing energy [78–80] or variance [81, 82]. The variance minimization is more robust, but energy minimization is often more accurate and more useful for optimizing parameters that alter the nodal surface of the wave function (see Sec. 3.2.2), such as the backflow parameters or coefficients of determinants [7]. The energy minimization is also shown in many cases to be more accurate for operators other than the Hamiltonian [83, 84]. This is also seen when estimating the positron lifetimes with all or most of the core electrons included in the calculation (see Publication I): the positron lifetimes are considerably improved when compared against experimental lifetimes if the wavefunctions are optimized with energy rather than variance minimization.

## 3.2 Diffusion Monte Carlo

### 3.2.1 Basic principles

Diffusion Monte Carlo (DMC) is among the most accurate methods in condensed matter physics. It considers the Schrödinger equation as a diffusion equation in

imaginary time $\tau$:

$$-\partial_\tau \left|\Phi(\mathbf{R},\tau)\right\rangle = \left(\hat{H} - E_T\right)\left|\Phi(\mathbf{R},\tau)\right\rangle, \tag{3.6}$$

where $\partial_\tau$ is the imaginary-time derivative and $\Phi(\mathbf{R},\tau)$ is the imaginary time- and space-dependent wave function of the system. $E_T$ is a control parameter, used for balancing the DMC stochastic process as explained below.

The basic idea of DMC is seen, if we write the solution of Eq. (3.6) as

$$\Phi(\mathbf{R},\tau) = \sum_{n=0}^{\infty} c_n \Psi_n e^{-(E_n - E_T)\tau} \tag{3.7}$$

relying on the separability of the time dependence in $\Phi$. Above, $\Psi_n$ and $E_n$ are the eigenstates and -energies of $\hat{H}$, and $c_n$ are linear coefficients of the eigenstates. The excited-state components of $\Phi$ are therefore exponentially decaying, and if we set $E_T = E_0$, the time dependence of $\Psi_0$ vanishes. In the limit $\tau \to \infty$ the excited-state components diminish to zero, leaving only $\Psi_0$, that is projected out of the initial wave function $\Phi(\mathbf{R}, \tau = 0)$.

The projection can be done by evolving an initial wave function $\Phi(\mathbf{R}, \tau = 0)$ in imaginary time. The initial wave function can in principle be any function of the coordinates $\mathbf{R}$ of the electrons, but in the studies of this work the initial wave function is a set of walkers, stochastically representing a VMC-optimized Slater-Jastrow wave function. The imaginary-time diffusion can be done by making repeatedly finite imaginary time steps to evolve the walkers. The steps for the walkers can be sampled from an approximate Green's function

$$\begin{aligned} G_{DMC}(\mathbf{R}' \to \mathbf{R}) = & \frac{1}{(2\pi\tau)^{3N/2}} \exp\left(-\frac{(\mathbf{R} - \mathbf{R}'))^2}{2\tau}\right) \\ & \times \exp\left(-\frac{\tau}{2}\left[V(\mathbf{R}) + V(\mathbf{R}') - 2E_T\right]\right) \end{aligned} \tag{3.8}$$

that is accurate with small time steps [5].

In Eq. (3.8), the first exponential is a Gaussian that is used to sample the steps made by the walkers from $\mathbf{R}$ to $\mathbf{R}'$. The average step size is determined by the imaginary time step $\tau$. The second exponential is dependent on the potential energy of the electron-ion and electron-electron (positron-ion and positron-electron) interactions, $V(\mathbf{R})$, for a given configuration $\mathbf{R}$. It is used to implement the so called branching process into the calculation. In the branching process, the walkers are spawned and killed at high- and low-potential regions, respectively. The control parameter $E_T$ is adjusted during the calculation to maintain the amount of walkers in the simulation around a target population.

### 3.2.2 Fixed-node approximation

The algorithm described in the previous section does not work in practice. This is due to the infamous fermion sign problem, that causes the statistics of a straightforward simulation of a fermionic system to be ill-behaved. The wavefunction of

the system has regions in configuration space that are either positive or negative. The representation of the wave function as a statistical ensemble of walkers cannot describe the regions of negative wave functions. The walkers can be assigned signs, that take into account the sign of the wave function appropriately, but this kind of solution easily causes the calculation to have exponentially decaying signal-to-noise ratio [5].

In this work the fixed-node approximation is used to overcome the sign problem: if a trial wave function is chosen, we can forbid the walkers to cross the nodal surface of a trial wavefunction. With $N$ particles in a 3-dimensional system, the wavefunction is $3N$-dimensional and it is zero in a $3N-1$-dimensional surface, the nodal surface. The wave function changes sign when the nodal surface is crossed, and thus the walkers can be restricted to areas with definite sign by killing the walkers attempting to cross the nodal surface. The application of the fixed-node approximation makes the evaluation of observables with DMC feasible, but introduces a bias dependent on the error in the nodal surface of the trial wave function. This is the main approximation of DMC; its accuracy is limited to the accuracy of the nodal surface of the trial wave function.

One important feature of fixed-node DMC is that energies computed are variational [85, 86]. This enables systematic improvement of the nodal surface of the trial wave function. There are multiple ways to improve nodal surfaces of these functions. One is to use the backflow function, as its optimization with respect to energy improves the nodal surface [71]. Other is to change the ways the single-particle orbitals are computed; the orbitals can be solved with HF or DFT, choosing different correlation functionals, and then the orbitals giving lowest DMC energies can be used. In the work on the NV center (article III), presented in this thesis, lots of attention is given to the best method to create the trial wave functions for DMC.

### 3.2.3 Importance sampling

Even with the fixed-node approximation the DMC as described so far is inefficient. The statistical fluctuations, especially with respect to walker population due to branching algorithm, are so large that great amount of computing power would be required to reach reasonable errorbars for the results. A solution for better performance is to sample, instead of the DMC wave function $\Phi$, another function $\psi = \Psi_T \Phi$, where $\Psi_T$ is a guiding wave function stabilizing the diffusion process [85, 87]. $\Psi_T$ is in this work the VMC-optimized Slater-Jastrow or Slater-Jastrow-backflow wave function, which is also used as the trial wave function that defines the nodal surface within the fixed-node approximation. We can determine the time evolution of $\psi$ by multiplying both sides of Eq. (3.6) with $\Psi_T$ to obtain a

modified Green's function for sampling the imaginary-time steps:

$$\begin{aligned}\tilde{G}_{DMC}(\mathbf{R}' \to \mathbf{R}) =& \frac{1}{(2\pi\tau)^{3N/2}} \exp\left(-\frac{(\mathbf{R}-\mathbf{R}'-\tau\mathbf{V}(\mathbf{R}'))^2}{2\tau}\right) \\ & \times \exp\left(-\frac{\tau}{2}\left[E_{loc}(\mathbf{R}) + E_{loc}(\mathbf{R}') - 2E_T\right]\right),\end{aligned} \tag{3.9}$$

where $E_{loc}$ is the VMC local energy and $\mathbf{V}(\mathbf{R})$ is the drift velocity

$$V(\mathbf{R}) = \frac{\nabla\Psi_T(\mathbf{R})}{\Psi_T(\mathbf{R})}. \tag{3.10}$$

The inclusion of the local energy in the Green's function causes the branching term to increase the probability of walker spawning in low local energy regions, and vice versa. The drift velocity makes the diffusion to favour directions where $|\Psi_T|$ increases. The use of importance-sampling in DMC greatly reduces the variations in local energy and population during the DMC process, thereby improving efficiency by reducing the statistical noise in the simulation.

As $\hat{H}_0\Phi_0 = E_0\Phi_0$, we can show also that the mixed estimate of the energy (energy with the guiding wave function) is equal to the pure estimate. After the equilibration we sample the distribution $f = \Phi_0\Psi_T$, and

$$\frac{\int \Phi_0(\mathbf{R})\Psi_T(\mathbf{R})E_{loc}(\mathbf{R})d\mathbf{R}}{\int \Phi_0(\mathbf{R})\Psi_T(\mathbf{R})d\mathbf{R}} = \frac{\langle\Phi_0|\hat{H}|\Psi_T\rangle}{\langle\Phi_0|\Psi_T\rangle} = E_0 = \frac{\langle\Phi_0|\hat{H}|\Phi_0\rangle}{\langle\Phi_0|\Phi_0\rangle} \tag{3.11}$$

The trial wave function restricts the DMC-wave function by its nodal surface, and hence the best possible estimate of the ground-state energy is the energy of the DMC wave function, with only nodal surface errors present.

For quantum mechanical operators that do not commute with the Hamiltonian, the mixed estimate does not correspond to the pure estimate. In these cases, with local $\hat{O}$ we can remove the first-order errors of the trial wave function present in the estimate by doing the following extrapolation [7]

$$\frac{\langle\Phi|\hat{O}|\Phi\rangle}{\langle\Phi|\Phi\rangle} \approx 2\frac{\langle\Phi|\hat{O}|\Psi_T\rangle}{\langle\Phi|\Psi_T\rangle} - \frac{\langle\Psi_T|\hat{O}|\Psi_T\rangle}{\langle\Psi_T|\Psi_T\rangle} + O((\Phi-\Psi_T)^2) \tag{3.12}$$

In practice, this means computing estimates of $\hat{O}$ with DMC and VMC, and taking the extrapolated estimate to be $\langle\hat{O}\rangle \approx 2\langle\hat{O}\rangle_{DMC} - \langle\hat{O}\rangle_{VMC}$. This has been done in the calculations of the electron-positron PCFs at zero distance in Publication I. For APMD this kind of extrapolation does not work, as evaluation of APMD is done with nonlocal operators.

## 3.3 Basis sets

Accurate, memory-efficient basis sets that can be evaluated without extensive computational cost are important in any quantum mechanical simulation. Plane-wave basis sets are used in this work with DFT, and the orbitals obtained are

then re-represented in a B-spline, or blip, real-space grid [88, 89] to speed up the QMC computations.

Plane-waves of the form $e^{i\mathbf{G}\cdot\mathbf{r}}$, with $\mathbf{G}$ a reciprocal lattice vector, are a natural basis for representation of Bloch orbitals. With $\mathbf{G}$ and $\mathbf{r}$ referring to the momentum and position of the wave, the exponential form exhibits periodicity. The number of plane-waves required for an accurate description of a given system varies, and is usually lower for DMC than for DFT. As increasing the simulation cell size densifies the momentum grid of the reciprocal lattice, more plane wave are needed for larger simulation cells. The computational cost of evaluating orbitals in plane-wave basis has cubic scaling with the number of plane-waves, posing severe restrictions to computational efficiency.

The use of blip basis functions [88] in QMC calculations largely removes the scaling problem of plane-waves. With blips, each orbital is evaluated in a local grid, making the cost of evaluating the wave function independent of system size [89], as in any $\mathbf{r}$ we have only 64 non-zero blip functions to evaluate. The blip coefficients can be obtained by fast-Fourier transforms from the plane-wave coefficients [89].

## 3.4 Vibrational effects

As mentioned in Sec. 2.1, we work within the Born-Oppenheimer approximation where the electronic structure is not dependent on nuclear motion. The equations of motion for the nuclei are obtained from the total energy $E(\{\mathbf{R}_I\})$, given by the Born-Oppenheimer Hamiltonian with nuclear coordinates $\mathbf{R}_I$ as parameters. In the equilibrium structure of a system, the total force acting on a nucleus is zero. This is the structure the system lies at most of the time, and therefore the structure most important for many of the system properties. Positron annihilation is often expected to happen in the ground state structure. Also vertical excitation energies of molecules and solid-state defects, measurable in experiments, are evaluated at the ground state structure.

However, the atoms display vibrational motion around the ground state even at zero temperature. This can affect the properties of the system, in which case the solution of the electronic Schrödinger equation within the Born-Oppenheimer approximation is not sufficient. The renormalization of the system properties with respect to lattice vibrations is an important phase in studies of properties dependent on electronic structure, as experimental observables compared against theory always include the effect of vibrations.

We now analyse the atomic vibrations in both zero and higher temperatures. Then a method is presented to renormalize the positron annihilation parameters studied in this work. Let $R^0_{k,\alpha}$ be a the $\alpha$th coordinate of the position of atom $k$ at equilibrium structure. By considering small atomic displacements around the

equilibrium structure $\mathbf{u}_k = \mathbf{R}_k - \mathbf{R}_k^0$, the energy $E(\{\mathbf{R}_I\})$ can be expanded with respect to the atomic positions at equilibrium structure as

$$E(\{\mathbf{R_I}\}) = E(\{\mathbf{R_I^0}\}) + \sum_{k,\alpha} \frac{\partial E(\{\mathbf{R}_I^0\})}{\partial R_{k,\alpha}} u_{k,\alpha} + \frac{1}{2} \sum_{k,\alpha,k',\alpha'} \frac{\partial^2 E(\{\mathbf{R}_I^0\})}{\partial R_{k,\alpha} \partial R_{k',\alpha'}} u_{k,\alpha} u_{k',\alpha'} + ... \tag{3.13}$$

Above, the second term gives the atomic forces, which are zero at equilibrium structure. The terms above second-order derivatives are neglected within the so-called harmonic approximation. By defining

$$\frac{\partial^2 E(\{\mathbf{R}_I^0\})}{\partial R_{k,\alpha} \partial R_{k',\alpha'}} = \Phi_{k,\alpha,k',\alpha'} \tag{3.14}$$

we get the classical equation of motion for the nuclei

$$M_k \frac{\partial^2 u_{k,\alpha}}{\partial t^2} = -\Phi_{k,\alpha,k',\alpha'} u_{k,\alpha} \tag{3.15}$$

Within the harmonic approximation, we can expect the atomic displacements to vibrate around the equilibrium positions as

$$u_{k,\alpha}(t) = \epsilon_{k,\alpha} e^{i\omega t}, \tag{3.16}$$

where $m$ is an oscillation mode. With this ansatz the equation of motion becomes

$$\sum_{k',\alpha'} \Phi_{k,\alpha,k',\alpha'} \epsilon_{k,\alpha} = M_k \omega^2 \epsilon_{k,\alpha}. \tag{3.17}$$

Now we can solve the vibrational modes as eigenvalues $\omega_m$ and -vectors $\epsilon_k^m$. This is easily done by evaluating $\Phi_{k,\alpha,k',\alpha'}$ with, e.g., linear response theory [90].

With the vibrational modes, atomic displacements can be stochastically sampled. If we compute a value of a quantum mechanical observable with each of the sampled structures and compute the average, we have an estimate of the observable expectation that includes also the vibrational effects within the harmonic approximation.

The sampling algorithm used in this work starts by drawing vibrational occupations for the vibrational states found by solving Eq. (3.19). The occupations are distributed according to the Boltzmann distribution:

$$p(m) \sim \frac{e^{-E_m/k_b T}}{\sum_j e^{-E_j/k_b T}}, \tag{3.18}$$

where $E_m$ denotes now the energy of the vibrational mode $m$. We can draw random samples of the occupations, distributed according to $p(m)$, by feeding uniformly distributed random variables between 0 and 1 to the inverse of the cumulative distribution function of $p(m)$. With $M$ samples for occupations of the vibrational modes, we can draw $M$ atomic displacements. For a vibrational

mode $n$, a displacement along the direction of the eigenvector of the mode is distributed according to the square of the wave function of a one-dimensional harmonic oscillator, written as

$$\Psi_n(x) = \frac{1}{\sqrt{a^n n!}} \left( \frac{M\omega_n}{\pi\hbar} \right)^{1/4} e^{-\frac{M\omega_n x^2}{2\hbar}} H_n \left( \sqrt{\frac{m\omega_n}{\hbar}} x \right), \tag{3.19}$$

where $H_n$ is a Hermite polynomial and $M$ refers to the mass of the atom we are computing the displacements for. If there are atoms with different masses, we have to, for a single vibrational mode, normalize the displacements according to the different masses of the atoms. The displacements can be sampled out of the square of the wave function of the harmonic oscillator with the Neumann algorithm.

During the course of this work an algorithm was programmed to sample the atomic displacements according to the theory and methods presented above. In the studies on positron lifetimes and Doppler broadening of the annihilation radiation in Si (found in Publications I and II), no changes are found when vibrational effects are included in the lifetime and momentum distribution estimates. This result may hold in other defect-free solids as well, but in future studies concerning positrons localized to lattice defects the vibrational effects may turn out to be important.

# Chapter 4

# Studies of positrons in solids

## 4.1 Overview

This chapter presents the theoretical study of positron annihilation in solids, with a focus on the use of QMC simulations to investigate the behaviour of positrons in crystalline diamond (C), aluminum nitride (AlN), silicon (Si), and lithium (Li). The focus is in the simulation of a single positron in the materials, as in positron experiments, only one positron is injected into a sample at a time. To establish a connection between the simulations and experimental observations, the positron lifetimes and momentum densities of the annihilating electron-positron pairs are calculated. This chapter presents the theory, computational developments, calculations, and results for these two properties of positron annihilation.

## 4.2 QMC with positrons

### 4.2.1 Hamiltonian

The inclusion of a positron into an electronic system complicates the Schrödinger equation, as there are now repulsive interactions between the positron and nuclei and, more importantly, there are both attractive and repulsive interactions present between the particles. The generalization of the Hamiltonian of the form in Eq. (2.2) can be expressed for systems with electrons and a single positron at $\mathbf{r}_+$ as

$$\begin{aligned}\hat{H} = &-\frac{1}{2}\sum_i \nabla_i^2 - \frac{1}{2}\nabla_+^2 - \sum_I \sum_i \frac{Z_I}{|\mathbf{r}_i - \mathbf{R}_I|} \\ &+ \sum_I \frac{Z_I}{|\mathbf{r}_+ - \mathbf{R}_I|} + \sum_i \sum_{j>i} \frac{1}{|\mathbf{r}_i - \mathbf{r}_j|} - \sum_i \frac{1}{|\mathbf{r}_i - \mathbf{r}_+|},\end{aligned} \tag{4.1}$$

where the second, fourth, and sixth term give the kinetic and electrostatic energies of the positron. We treat cases of only single positron present in the system because that is the case usually in positron experiments.

### 4.2.2 Wave function

To include positron in the wave function simulated with QMC, we can use Slater-Jastrow wave function of the form in Eq. (2.19), and include positron as a "third spin component":

$$\begin{aligned}\Psi^{SJ}(\mathbf{r}_+;\mathbf{r}_1,\mathbf{r}_2,...,\mathbf{r}_N)\\ = e^{J(\mathbf{r}_+,\mathbf{r}_1,\mathbf{r}_2,...\mathbf{r}_N)}D^{\uparrow}(\mathbf{r}_1,\mathbf{r}_2,...\mathbf{r}_{N_\uparrow})D^{\downarrow}(\mathbf{r}_{N_\uparrow+1},\mathbf{r}_{N_\uparrow+2},...\mathbf{r}_{N_\uparrow+N_\downarrow})D^{+}(\mathbf{r}_+)\end{aligned} \tag{4.2}$$

Above, we have omitted the use of particle coordinates $x_i$ including spin, and are using the spatial coordinates with the first $N^{\uparrow}$ coordinates corresponding to spin-up electrons, and the rest to spin-down electrons. $\mathbf{r}_+$ corresponds to the positron coordinate. We have omitted the sum over different determinants, as in the positron studies done in this work only one determinant is used to define systems' wavefunctions. Also we only consider systems with a single positron, although the treatment of systems with multiple positrons should be straightforwardly generalized from this analysis. Because of only a single positron present, the positron determinant $D^+$ reduces to the positron orbital $\phi^+$.

The Jastrow factor and the backflow function are generalized for electron-positron wave functions by introducing new components for the one-, two-, and three-body terms corresponding to new grouping indices in $P$, $S$, and $T$ in Eqs. (2.14) and (2.21). The new groups correspond to the electron-positron and nucleus-positron pairs.

Figure 4.1 presents the optimized $u$- and $\chi$-terms of the Jastrow factor, also shown in Publication I for the wave functions of positron embedded in bulk C, AlN, Si, and Li. There are three $u$-terms for each system as the particle groupings have been defined so that separate terms are given to particles with different charge or spin. Also for the $\chi$-term we have given separate terms for the interactions of electrons and the positron with each of the nuclei type in the system.

Publication I discusses the details of Fig. 4.1 further. It should be noted, however, that there is a close correspondence between the electron-positron $u$-term in the Jastrow factor and the electron-positron pair correlation functional. The $u$-term is therefore the most important factor in the simulations for capturing the positron correlations. The correlations at contact are especially important, as they mainly determine the features of annihilation.

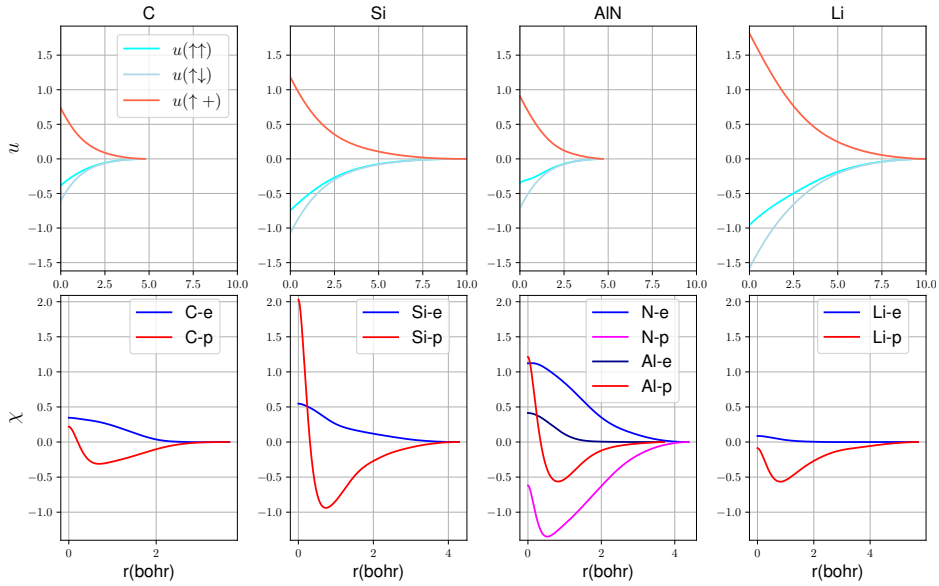


Figure 4.1: The $u$- and $\chi$-terms of the optimized Jastrow factors in QMC simulations of Slater-Jastrow-backflow wave functions in bulk C, AlN, Si, and Li. The $u$-terms are optimized separately for parallel- and antiparallel-spin electron pairs, and for electron-positron pairs without spin dependence. The $\chi$-terms are optimized separately for electron- and positron-nucleus pairs, with separate terms for each of the nuclei type present in the simulation cell. Figure taken from publication I. Copyright © 2022 by American Physical Society. All rights reserved.

### 4.2.3 Positron-nucleus interactions

In the QMC simulations with positrons, we ended up treating the positron-nucleus interactions in pseudopotential calculations by multiplying the pseudopotential by $-1$ for positrons. We also tried to simulate the wavefunctions with positrons with just Coulombic interactions between the positron and the positively charged nuclei, but since this provided the same results as with using inverted electron pseudopotentials for the positron-nucleus interactions, we chose the latter method to have the treatment of electron-nucleus and positron-nucleus interactions symmetric with respect to particle charge.

### 4.2.4 Nodal surface and fixed-node error

The positron orbital for QMC simulations is solved within the level of a single-particle theory. It has the form of a Bloch orbital for free positron, which resembles that of electrons, and is always sampled with zero wave vector $\mathbf{k}_+ = 0$, as we have only one positron and we assume it to set to the lowest available $s$-type nodeless orbital. Hence the form of the positron orbital given to the trial wave function in Publications I-II for QMC simulations does not change the positron

state projected out by the DMC algorithm, even thought the correct form improves the statistics.

## 4.3 Positron Annihilation

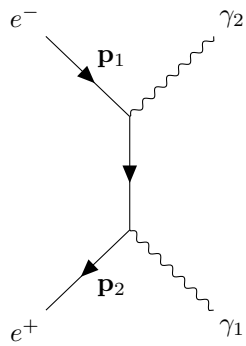


Figure 4.2: The second-order process of positron annihilation, expressed as a Feynman graph with time flowing from left to right. The annihilation releases two photons $\gamma_1$ and $\gamma_2$ after a collision of an electron ($e^-$) and a positron ($e^+$) with momenta $\mathbf{p}_1$ and $\mathbf{p}_1$, respectively. The total momentum $\mathbf{p} = \mathbf{p}_1 + \mathbf{p}_2$ is conserved, so that the total momenta of the photons is also $\mathbf{p}$. This second-order process can happen with opposite-spin electron-positron pairs, and is much more common than higher-order annihilation processes.

### 4.3.1 Annihilator operator

The annihilation process in a positron-electron system evolves the state of the initial system $|i\rangle$ into a state of the final system $|f\rangle$, where the former includes $N$ electrons and a positron and the latter $N-1$ electrons. The total momentum $\mathbf{p}$ of the annihilating electron-positron pair is the sum of the electron and positron momenta $\mathbf{p}_1$ and $\mathbf{p}_2$ at the moment of annihilation (see Fig. 4.2). The second-order annihilation process, which we focus on in this study, involves electron-positron pairs of opposite spins, and releases two annihilation photons $\gamma_1$ and $\gamma_2$ with total momentum $\mathbf{p}$. The average energy of both of the photons is 511 keV according to Einstein's mass-to-energy relation, and the energy of the individual photons is distributed according to the distribution of $\mathbf{p}_1 + \mathbf{p}_2$. The higher-order processes, releasing three or more photons, may involve spin-parallel electron-positron pairs but are much less probable.

If we work in the scheme of the second quantization, we can define the annihilation operators $a_{\mathbf{p}_1}$ and $b_{\mathbf{p}_2}$ that, when operated on a wave function, destroy electron with momentum $\mathbf{p}_1$ and positron with momentum $\mathbf{p}_2$. The rate of annihilations resulting to the creation of a photon pair with momentum $\mathbf{p} = \mathbf{p}_1 + \mathbf{p}_2$ is given

as [91, 92]

$$\begin{aligned}\Gamma(\mathbf{p}) =& \pi r_0^2 c \sum_f \left| \langle f | \sum_{\mathbf{p}_1,\mathbf{p}_2} a_{\mathbf{p}_1} b_{\mathbf{p}_2} \delta_{\mathbf{p}_1+\mathbf{p}_2,\mathbf{p}} | i \rangle \right|^2 \\ =& \pi r_0^2 c \sum_f \left| \langle f | \hat{O}(\mathbf{p}) | i \rangle \right|^2,\end{aligned} \tag{4.3}$$

where $\pi r_0^2 c$ is the so called Dirac ratio, that gives the quantum electrodynamic cross-section for the annihilation of an electron-positron pair with zero total spin. The squared part corresponds to the wave function-based probabilities of electron-positron collisions, summed over electron and positron momenta [13, 93]. The above formula does not include explicit treatment of spins, but works for cases where the electronic subsystem has zero total spin.

By defining the annihilator operators in a field-theoretic form as

$$a_{\mathbf{p}} = \frac{1}{\sqrt{V}} \int e^{-i\mathbf{p}\cdot\mathbf{r}} \hat{\phi}(\mathbf{r}) d\mathbf{r} \tag{4.4}$$

$$b_{\mathbf{p}} = \frac{1}{\sqrt{V}} \int e^{-i\mathbf{p}\cdot\mathbf{r}} \hat{\psi}(\mathbf{r}) d\mathbf{r}, \tag{4.5}$$

where $\hat{\phi}(\mathbf{r})$ ($\hat{\psi}(\mathbf{r})$) annihilates an electron (positron) at point $\mathbf{r}$, we get

$$\begin{aligned}\hat{O}(\mathbf{p}) &= \sum_{\mathbf{p}_1,\mathbf{p}_2} \frac{1}{\sqrt{V}} \int e^{-i\mathbf{p}_1\cdot\mathbf{r}_1} \hat{\phi}(\mathbf{r}_1) d\mathbf{r}_1 \frac{1}{\sqrt{V}} \int e^{-i\mathbf{p}_2\cdot\mathbf{r}_2} \hat{\psi}(\mathbf{r}_2) d\mathbf{r}_2 \delta_{\mathbf{p}_1+\mathbf{p}_2,\mathbf{p}} \\ &= \sum_{\mathbf{p}_1} \frac{1}{\sqrt{V}} \int e^{-i\mathbf{p}_1\cdot\mathbf{r}_1} \hat{\phi}(\mathbf{r}_1) d\mathbf{r}_1 \frac{1}{\sqrt{V}} \int e^{-i(\mathbf{p}-\mathbf{p}_1)\cdot\mathbf{r}_2} \hat{\psi}(\mathbf{r}_2) d\mathbf{r}_2 \\ &= \frac{1}{V} \sum_{\mathbf{p}_1} \int\int e^{-i\mathbf{p}_1\cdot(\mathbf{r}_1-\mathbf{r}_2)} e^{-i\mathbf{p}\cdot\mathbf{r}_2} \hat{\phi}(\mathbf{r}_1) \hat{\psi}(\mathbf{r}_2) d\mathbf{r}_1 d\mathbf{r}_2 \\ &= \int\int \delta(\mathbf{r}_1-\mathbf{r}_2) e^{-i\mathbf{p}\cdot\mathbf{r}_2} \hat{\phi}(\mathbf{r}_1) \hat{\psi}(\mathbf{r}_2) d\mathbf{r}_1 d\mathbf{r}_2 \\ &= \int e^{-i\mathbf{p}\cdot\mathbf{r}} \hat{\phi}(\mathbf{r}) \hat{\psi}(\mathbf{r}) d\mathbf{r},\end{aligned} \tag{4.6}$$

where in the third line we have taken the continuum limit $\frac{1}{V}\sum_{\mathbf{p}} \to \frac{1}{(2\pi)^3}\int d\mathbf{p}$ and used the identity $\frac{1}{(2\pi)^3}\int e^{i\mathbf{p}(\mathbf{r}-\mathbf{r}')} d\mathbf{p} = \delta(\mathbf{r}-\mathbf{r}')$, and in the last line we have interchanged $\mathbf{r}_1$ to $\mathbf{r}$ for convenience. This form of the annihilator operator $\hat{O}(\mathbf{p})$ is used in evaluating expressions for the positron lifetime and annihilating-pair momentum density (APMD) utilized by QMC algorithms in this work.

### 4.3.2 Positron lifetime

#### Theoretical formulation

The annihilation rate of the positron in a given initial system $|i\rangle$ normalized to one positron per unit volume is given by integrating over $\mathbf{p}$ in Eq. (4.3):

$$\begin{aligned}\Gamma &= \int \Gamma(\mathbf{p})\frac{d\mathbf{p}}{(2\pi)^3} = \int \sum_f \langle i|\hat{O}(\mathbf{p})^\dagger|f\rangle\langle f|\hat{O}(\mathbf{p})|i\rangle\frac{d\mathbf{p}}{(2\pi)^3} = \int \langle i|\hat{O}(\mathbf{p})^\dagger\hat{O}(\mathbf{p})|i\rangle\frac{d\mathbf{p}}{(2\pi)^3} \\ &= \int \langle i|\left[\int e^{i\mathbf{p}\cdot\mathbf{r}}\hat{\phi}^\dagger(\mathbf{r})\hat{\psi}^\dagger(\mathbf{r})d\mathbf{r}\right]\left[\int e^{-i\mathbf{p}\cdot\mathbf{r}'}\hat{\phi}(\mathbf{r}')\hat{\psi}(\mathbf{r}')d\mathbf{r}'\right]|i\rangle\frac{d\mathbf{p}}{(2\pi)^3} \\ &= \langle i|\int\int \delta(\mathbf{r}-\mathbf{r}')\hat{\phi}^\dagger(\mathbf{r})\hat{\psi}^\dagger(\mathbf{r})\hat{\phi}(\mathbf{r}')\hat{\psi}(\mathbf{r}')d\mathbf{r}d\mathbf{r}'|i\rangle \\ &= \langle i|\int \rho_e(\mathbf{r})\rho_p(\mathbf{r})d\mathbf{r}|i\rangle\end{aligned} \tag{4.7}$$

Above, the Dirac ratio $\pi r_0^2 c$ is omitted for readability. Also, to correctly treat the spin of the particles we should apply a spin projection operator $\hat{O}_s$ to the operator within brakets in order to restrict our consideration to the annihilations of electron-positron pairs with opposite spins. For systems with zero total electronic spin this corresponds to multiplying the formula above with 1/2. $\hat{\phi}^\dagger(\mathbf{r})\hat{\phi}(\mathbf{r}) = \rho_e(\mathbf{r})$ ($\hat{\psi}^\dagger(\mathbf{r})\hat{\psi}(\mathbf{r}) = \rho_p(\mathbf{r})$) represents the density operator of electrons (positron) at site $\mathbf{r}$, formally given as $\rho_e(\mathbf{r}) = \sum_i^{N_e}\delta(\mathbf{r}-\mathbf{r}_i)$. From Eq. (4.3) we can see that the annihilation rate of the positron in a given system, described by $|i\rangle$, is given by integrating the electron density at positron's site over the entire system. Hence the 2-photon annihilation rate is connected to the overlap of electrons and the positron via the Dirac ratio.

#### Lifetime calculations prior to this work

As mentioned, the simulation of positrons trapped to solid-state defects has so far been only possible in the framework of DFT. DFT is also the main workhorse for studies of bulk solids, although many-body methods have also been tried out [94]. The annihilation rate $\Gamma$, i.e., the inverse of the lifetime $\tau$, is calculated with DFT using the self-consistent charge densitites for the electrons, $n_-(\mathbf{r})$, and for the positron, $n_+(\mathbf{r})$, as [28]

$$\Gamma = \frac{1}{\tau} = \pi r_0^2 c\int d\mathbf{r} n_-(\mathbf{r})n_+(\mathbf{r})g(\mathbf{r},\mathbf{r};[n_-,n_+]) \tag{4.8}$$

Above, the factor $g(\mathbf{r},\mathbf{r};[n_-,n_+])$ is the electron-positron pair correlation function at zero electron-positron distance, expressed as a functional of electron and positron densities. This term is called the enhancement factor, and it accounts for the short-ranged screening of the positron by electrons that is not included in the one-body densities.

A usual approximation in evaluating Eq. (4.8) is to take zero-positron-density limit. Then the enhancement factor can be approximated within LDA as $g(\mathbf{r},\mathbf{r};[n_-,n_+]) \to \gamma(n_-(\mathbf{r}))$ [14]. This kind of enhancement factor $\gamma$ can be evaluated by, e.g., evaluating electron-positron PCF at zero distance in homogenous electron gas with varying electron density, and fitting a polynomial to the obtained results, as is done in Ref. [36].

Many-body theory has been used previously in estimating positron lifetimes, or annihilation rates, in homogenous electron gas [95, 96] and in atoms [97]. QMC has also been used for the estimation of positron lifetimes in homogenous electron gas [36]. However, these methods have not been applied directly to solids, which are the focus of the present work.

**Lifetime calculations with quantum Monte Carlo**

Evaluating the expression of the annihilation rate in Eq. (4.7) further, by choosing a wave function as $\Psi(\mathbf{r}_+;\mathbf{r}_1,...,\mathbf{r}_N)$, where $\mathbf{r}_+$ is the positron's position and $\mathbf{r}_i$ represents the position of electron $i$, we can connect it with the electron-positron density matrix:

$$\begin{aligned}
\Gamma &= \langle\Psi(\mathbf{r}_+;\mathbf{r}_1,...,\mathbf{r}_N)| \int \hat{\phi}^\dagger(\mathbf{r})\hat{\psi}^\dagger(\mathbf{r})\hat{\phi}(\mathbf{r})\hat{\psi}(\mathbf{r})d\mathbf{r}|\Psi(\mathbf{r}_+;\mathbf{r}_1,...,\mathbf{r}_N)\rangle \\
&= \int \langle\Psi(\mathbf{r}_+;\mathbf{r}_1,...,\mathbf{r}_N)| \sum_{i=1}^{N} \delta(\mathbf{r}-\mathbf{r}_i)\delta(\mathbf{r}-\mathbf{r}_+)|\Psi(\mathbf{r}_+;\mathbf{r}_1,...,\mathbf{r}_N)\rangle d\mathbf{r} \\
&= \int N\langle\Psi(\mathbf{r};\mathbf{r},...,\mathbf{r}_N)|\Psi(\mathbf{r};\mathbf{r},...,\mathbf{r}_N)\rangle d\mathbf{r} \\
&= \int N\left[\int \Psi^*(\mathbf{r};\mathbf{r},\mathbf{r}_2...,\mathbf{r}_N)\Psi(\mathbf{r};\mathbf{r},\mathbf{r}_2,...,\mathbf{r}_N)d\mathbf{r}_2,...,d\mathbf{r}_N\right] d\mathbf{r} \\
&= \int \gamma_{ep}(\mathbf{r},\mathbf{r};\mathbf{r},\mathbf{r})d\mathbf{r},
\end{aligned} \tag{4.9}$$

where the electron-positron density matrix $\gamma_{ep}(\mathbf{r}_1,\mathbf{r}_2;\mathbf{r}_3,\mathbf{r}_4)$ is defined as

$$\gamma_{ep}(\mathbf{r}_1,\mathbf{r}_2;\mathbf{r}_3,\mathbf{r}_4) = N\int \Psi^*(\mathbf{r}_1;\mathbf{r}_2,\mathbf{r}'_3...,\mathbf{r}'_N)\Psi(\mathbf{r}_3;\mathbf{r}_4,\mathbf{r}'_3,...,\mathbf{r}'_N)d\mathbf{r}'_3,...,d\mathbf{r}'_N \tag{4.10}$$

and, when only electron-positron pairs of antiparallel spin are considered, can be restricted to spin-down positron at $\mathbf{r}_1$ and $\mathbf{r}_3$ and spin-up electron at $\mathbf{r}_2$ and $\mathbf{r}_4$.

The diagonal elements of the pair density satisfy the relation

$$\gamma_{ep}(\mathbf{r}_1,\mathbf{r}_2;\mathbf{r}_1,\mathbf{r}_2) = n_e(\mathbf{r}_1)n_p(\mathbf{r}_2)g_{ep}(\mathbf{r}_1,\mathbf{r}_2), \tag{4.11}$$

were $n_e$ ($n_p$) represents the one-body density of electrons (positrons). $g_{ep}(\mathbf{r}_1,\mathbf{r}_2)$ is called the pair correlation function, as already presented in Eq. (2.11) for particle types $\sigma_i$ and $\sigma_j$. With $\mathbf{r}_1 = \mathbf{r}_2$ Eq. (4.11) is also said to define the contact density $\gamma_{ep}(\mathbf{r}_1,\mathbf{r}_1;\mathbf{r}_1,\mathbf{r}_1)$. The contact density at $\mathbf{r}$ is a product of the

$n_e$ and $n_p$ at the given coordinates, multiplied by $g_{ep}(0;\mathbf{r})$, which is the electron-positron PCF at zero electron-positron distance, evaluated at $\mathbf{r}$.

The integration of the contact density over $\mathbf{r}$ in a periodic simulation cell can be done with the mean value theorem for integrals, and gives

$$\int \gamma_{ep}(\mathbf{r},\mathbf{r};\mathbf{r},\mathbf{r})d\mathbf{r} = \frac{N}{V} g_{ep}(0), \tag{4.12}$$

where $g_{ep}(0)$ is the value of the electron-positron PCF at zero electron-positron distance, averaged over the simulation cell. It can also be interpreted as the zero-distance value of the spherically and translationally averaged electron-positron PCF $g_{ep}(|\mathbf{r}_1 - \mathbf{r}_2)|$.

Now we can see that the problem of calculating positron lifetimes can be reduced to the problem of evaluating the $g_{ep}(0)$, as the lifetime $\tau$ is the inverse of the annihilation rate. Combining Eqs. (4.9) and (4.12), and including the Dirac ratio omitted for readability since Eq. (4.7), gives

$$\tau^{-1} = \Gamma = \pi r_0^2 c \frac{N}{V} g_{ep}(0). \tag{4.13}$$

We should note in the above equation, that if the spin-projection operator $\hat{O}_s$ would be applied correctly in the annihilation operator, the above formula would apply only on the electronic density $\frac{N}{V}$ of opposite spin to the positron. We can obtain a stochastic estimate of $g(|\mathbf{r}_1 - \mathbf{r}_2|)$ during a QMC simulation by collecting electron-positron distances in bins while sampling a trial wave function $\Psi$ during VMC or DMC simulation. The binning method defines the spherical pair correlation function as a function of discrete distances $|\mathbf{r}_1 - \mathbf{r}_2|_n$, which represent (e.g.) centers of bins of width $\Delta$:

$$g_{ep}(|\mathbf{r}_1 - \mathbf{r}_2)|_n) = \frac{V_n}{V} \left\langle \frac{N_{ep}^n}{N_e} \right\rangle, \tag{4.14}$$

where $V_n$ is the volume of bin $n$, and $N_{ep}^n$ is the number of electron-positron separations that lie within the distance range of the $n$th bin in a given configuration. Best results for $g_{ep}(|\mathbf{r}_1 - \mathbf{r}_2)|_n)$ are obtained with extrapolated estimation (see Sec. 3.2.3).

### 4.3.3 Analysis of the pair correlation function data

The QMC sampling process of the PCF gives noisy data near the region $|\mathbf{r}_1 - \mathbf{r}_2| \approx 0$, so that we cannot directly estimate $g(0)$ from the QMC data. Instead, we must fit a polynomial to the spherical pair correlation function data in order to get a robust estimate of $g(0)$ [36]. The first-order coefficient of the polynomial should be fixed to $-1$ to ensure that the fit satisfies the Kimball cusp conditions [98].

Figure 4.3 shows a $g(0)$ histogram, representing translationally and rotationally averaged PCF of an electron-positron pair, accumulated with QMC in a Si 16-atom simulation cell. It clearly shows how the data gets noisy close to zero

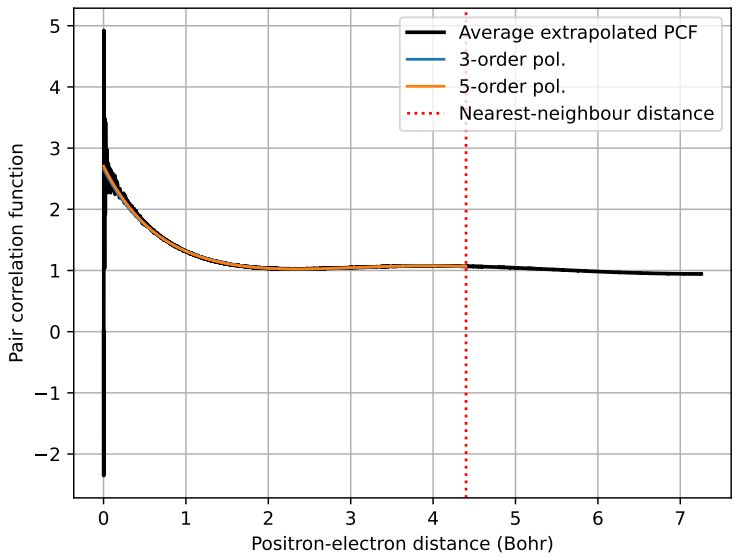


Figure 4.3: Black line: QMC data of spherically and translationally averaged PCF in 16-atom Si simulation cell, obtained with a Slater-Jastrow wave function, as a function of the electron-positron distance. Blue and orange lines show 3rd- and 5th-order polynomial fits against the PCF data, fitted below distances corresponding to nearest-neighbour atom distance in the simulation cell. Figure taken from Publication I. Copyright © 2022 by American Physical Society. All rights reserved.

distance. Fig. 4.3 also shows polynomial fits with polynomial orders 3 and 5 against the PCF data. The fits are done in the region below nearest-neighbour distance of the atoms in the simulation cell. This region and the polynomial order of 5 were chosen for all of the PCF results from different materials, simulation cell sizes and wave functions with and without the backflow. The decision was based on a cross-validation analysis, where fitting errors were compared between independent PCF results of the same material, simulation cell and wave function level. The independence of the data in cross-validation was ensured by using different twist vectors when preparing the wave functions.

To obtain a statistical errorbar for the obtained $g(0)$, we perform multiple independent QMC simulations to obtain a set of $g(0)$ estimates, and take the mean and standard deviation of the set as the best estimate and statistical error. As the independent simulations are performed with different twist vectors, this process produces a twist-averaged estimate.

It should be mentioned that the results can be greatly improved with extrapolated estimation of $g(0)$ (see Sec. 3.2.3).

### 4.3.4 Annihilating-pair momentum density

#### Prior work

The experimental positron annihilation Doppler spectra, which are the 1D projections of the APMD, have been previously calculated with many-body theories in ions and atoms [92, 97], and in electron gas [36], and there are some studies for bulk solids [94]. However, defected solids, the simulation of which is the aim of this work, have been only studied in DFT level with respect to APMD and Doppler spectra.

In DFT framework one can use the enhancement factor to formulate an expression for the annihilating-pair momentum density (APMD) as

$$\Gamma(\mathbf{p}) = \pi r_0^2 c \sum_j \left| \int d\mathbf{r} e^{-i\mathbf{p}\cdot\mathbf{r}} \psi_+(\mathbf{r}) \psi_j(\mathbf{r}) \sqrt{\gamma(n_-(\mathbf{r}))} \right|^2 , \tag{4.15}$$

where $\psi_+$ and $\psi_j$ refer to the positron and to the $j$th electron orbital, and $\gamma$ is the enhancement factor. This form for the calculation of the APMD is referred to as the state-independent model.

An alternative formulation is to use the state-dependent model, where the APMD is evaluated as

$$\Gamma(\mathbf{p}) = \pi r_0^2 c \sum_j \gamma_j \left| \int d\mathbf{r} e^{-i\mathbf{p}\cdot\mathbf{r}} \psi_+(\mathbf{r}) \psi_j(\mathbf{r}) \right|^2 , \tag{4.16}$$

where $\gamma_j = \lambda_j^{LDA}/\gamma_j^{IPM}$ and

$$\lambda_j^{LDA} = \pi r_0^2 c \int d\mathbf{r} \left|\psi_+(\mathbf{r})\right|^2 \left|\psi_j(\mathbf{r})\right|^2 \sqrt{\gamma(n_-(\mathbf{r}))}. \tag{4.17}$$

$\gamma_j^{IPM}$ is evaluated as $\gamma_j^{LDA}$ but with $\gamma$ set to one [14].

Neither of the above models for the APMD is theoretically sound. They attempt to capture the APMDs with approximative formulations that are not directly linked to the fundamental theory. Below, an explicit and theoretically correct formulation for APMD is derived along with an implementation for evaluating it with QMC.

#### Theory and implementation to quantum Monte Carlo

The APMD $\Gamma(\mathbf{p})$ is already given in Eq. (4.3), but it must be reformulated for QMC estimation. We start from the second line of Eq. (4.7), substituting $|i\rangle$ with wavefunctions $\Psi(\mathbf{r}_+; \mathbf{r}_1, ..., \mathbf{r}_N)$, and by removing the integration over momentum

we get (excluding the spin projection operator for simplicity)

$$
\begin{aligned}
\Gamma(\mathbf{p}) = & \\
& \langle \Psi(\mathbf{r}_+; \mathbf{r}_1, ..., \mathbf{r}_N)| \int\int e^{-i\mathbf{p}\cdot(\mathbf{r}'-\mathbf{r})} \hat{\phi}^\dagger(\mathbf{r})\hat{\psi}^\dagger(\mathbf{r}) \\
& \times \hat{\phi}(\mathbf{r}')\hat{\psi}(\mathbf{r}') d\mathbf{r} d\mathbf{r}' |\Psi(\mathbf{r}_+; \mathbf{r}_1, ..., \mathbf{r}_N)\rangle \\
= & \int\int \sum_{i=1}^{N} \langle \Psi(\mathbf{r}_+; \mathbf{r}_1, ..., \mathbf{r}', ..., \mathbf{r}_N)|\delta(\mathbf{r}-\mathbf{r}_i) \\
& \times \delta(\mathbf{r}'-\mathbf{r}_+) e^{-i\mathbf{p}\cdot(\mathbf{r}'-\mathbf{r})} |\Psi(\mathbf{r}; \mathbf{r}_1, ..., \mathbf{r}_N)\rangle d\mathbf{r} d\mathbf{r}' \\
= & \sum_{i=1}^{N} \langle \Psi(\mathbf{r}_+; \mathbf{r}_1, ..., \mathbf{r}_+, ..., \mathbf{r}_N)|e^{-i\mathbf{p}\cdot(\mathbf{r}_+-\mathbf{r}_i)}|\Psi(\mathbf{r}_i; \mathbf{r}_1, ..., \mathbf{r}_i, ..., \mathbf{r}_N)\rangle \\
= & N \int\int\int ... \int \Psi^*(\mathbf{r}_+; \mathbf{r}_+, ..., \mathbf{r}_N)\Psi(\mathbf{r}_1; \mathbf{r}_1, ..., \mathbf{r}_N) e^{-i\mathbf{p}\cdot(\mathbf{r}_+-\mathbf{r}_1)} d\mathbf{r}_+ d\mathbf{r}_1 d\mathbf{r}_2 ... \mathbf{r}_N \\
= & N \int\int\int ... \int |\Psi(\mathbf{r}_+; \mathbf{r}_1, ..., \mathbf{r}_N))|^2 \\
& \times \frac{\Psi^*(\mathbf{r}_+; \mathbf{r}_+, ..., \mathbf{r}_N)}{\Psi(\mathbf{r}_+; \mathbf{r}_1, ..., \mathbf{r}_N)} \frac{\Psi(\mathbf{r}_1; \mathbf{r}_1, ..., \mathbf{r}_N)}{\Psi(\mathbf{r}_+; \mathbf{r}_1, ..., \mathbf{r}_N)} e^{-i\mathbf{p}\cdot(\mathbf{r}_+-\mathbf{r}_1)} d\mathbf{r}_+ d\mathbf{r}_1 d\mathbf{r}_2 ... \mathbf{r}_N,
\end{aligned}
\tag{4.18}
$$

where the last line is an integration formula of the form in Eq. (3.3), meaning that we can define

$$
\Gamma(\mathbf{p}) = \pi r_0^2 c N \left\langle \Psi \left| \frac{\Psi(\mathbf{r}_+; \mathbf{r}_+, ..., \mathbf{r}_N)}{\Psi(\mathbf{r}_+; \mathbf{r}_1, ..., \mathbf{r}_N)} \frac{\Psi(\mathbf{r}_1; \mathbf{r}_1, ..., \mathbf{r}_N)}{\Psi(\mathbf{r}_+; \mathbf{r}_1, ..., \mathbf{r}_N)} e^{-i\mathbf{p}\cdot(\mathbf{r}_+-\mathbf{r}_1)} \right| \Psi \right\rangle \tag{4.19}
$$

Thus the evaluation of the APMD can be done with a VMC simulation, where we estimate ratios of wave functions during the sampling process. In the first ratio, an electron is moved on top of the positron in the numerator, and in the second ratio the positron is moved on top of an electron. The denominator in both ratios is the wave function value with a given configuration. The **p**-grid in which the APMD is evaluated must be dense enough in order for it to be meaningfully compared against experiments. The grid can be densified either by increasing simulation cell size, or by twist averaging (see Sec. 2.4.1). Because of small finite-size effects of APMD, the latter method proved to be more efficient. Results of different twists can also be used in evaluating statistical error for the APMD results.

The accumulation of the $\Gamma(\mathbf{p})$ as given in Eq. (4.19) can be done only in the VMC level; a stochastically sampled DMC wave function would still need an expression for the wave function to estimate the APMD, which is not given by DMC. Hence, in DMC, we would need to use VMC wave functions for the estimation of the ratios in Eq. (4.19). The errors in the VMC wave function cannot be reduced by extrapolation schemes such as in lifetime calculations for local operators, and hence we would have an uncharacterized error in APMDs estimated with DMC. Publication II shows that at least in pristine Si and AlN VMC provides very accurate Doppler spectra.

**Postprocessing and Doppler broadening of the annihilation radiation**

Publication II contains results of the APMD, compared against Doppler broadening experiments of positron annihilation radiation, in C, Si and AlN. The experimental data available contained 1D projections $\rho(p_L)$, along the longitudinal component of the momentum towards a detector, of the Doppler broadening, defined as

$$\rho(p_L) = \int\int \Gamma(\mathbf{p}) dp_y dp_z, \tag{4.20}$$

This kind of 1D spectra results from the use of 1 or 2 detectors around the sample, placed exactly opposite to one another. To estimate $\rho(p_L)$ from our VMC-estimated $\Gamma(\mathbf{p})$, we have to numerically evaluate Eq. (4.20).

The evaluation is done with linear interpolation method. It requires us to first fill the space of $\mathbf{G}_i$ with non-intersecting tetrahedra. This is done with a Delaunay tetrahedralization algorithm, that finds the tetrahedralization where the tetrahedra have maximally large internal angles, hence making the succeeding interpolation as robust as possible. In principle Delaunay tetrahedralization creates tetrahedra filling a point cloud with as little "spikes" or "sharp angles" as possible. After the tetrahedralization, we use linear interpolation method, as defined in [99], to obtain $\rho(p_L)$.

## 4.4 Results

### 4.4.1 Lifetime results from quantum Monte Carlo simulations

In Publication I, we estimate the $g(0)$ in C, Si, AlN, and Li. We alter the simulation cell sizes to explore finite-size effects (see Sec. 2.4.1), and we test different pseudopotentials (Sec. 2.5) and all-electron calculations to estimate how important it is to include core electrons to the estimation of $g(0)$. We also include a backflow correction to the results (Sec. 2.3.5). The results are presented in Figure 4.4.

Figure 4.4 also presents the lifetime results obtained with previous state-of-the-art methods (see Sec. 2.2.1 and discussion on lifetime calculations before this work above in this chapter.). These methods, listed according to the enhancement factors used to model the correlation effects, are: Drummond *et al.* LDA (D-LDA)[36], Boroński-Nieminen LDA (BN-LDA)[28], Kuriplach-GGA (KUR-GGA)[30], and GGAs by Barbiellini *et al.* from Ref. [29] (B95-GGA) and [31] (B15-GGA). B15-GGA was also used to estimate the annihilation rate due to core electrons, which is not included in the QMC simulations due to the use of pseudopotentials, except in the case of the all-electron Li simulation. Hence the

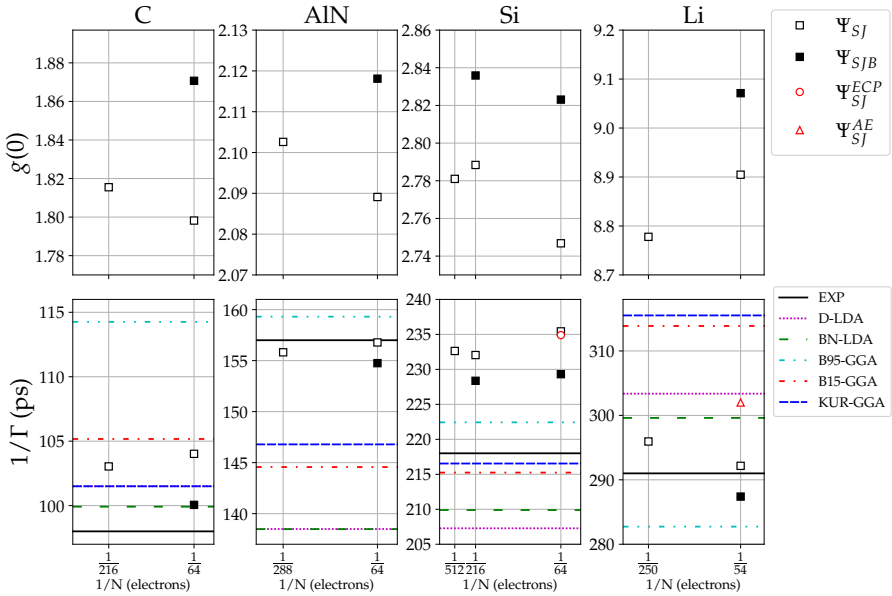


Figure 4.4: $g(0)$ results (top row), and lifetimes (bottom row) for C, AlN, Si, and Li. The figure shows twisted Slater-Jastrow (empty square) and Slater-Jastrow-backflow (full square) wave function results with AREP pseudopotentials as well as the ECP pseudopotential (red circle) and all-electron Slater-Jastrow results (red triangle) as a function of the inverse of the number of electrons in the simulation. The ECP-pseudopotential and all-electron results are compared against AREP results with the same cell sizes. Monte Carlo errorbars were drawn for each result, but they are smaller than the PCF and lifetime datapoints. We present the lifetime estimates against experiment (black solid line) for C [100], AlN [101], Si [102], and Li [103]. We also computed DFT lifetime estimates with different positron correlation functionals (dash-dotted lines): D-LDA (violet) [36], BN-LDA (green) [28], B95-GGA (cyan) [29], B15-GGA (red) [31], and KUR-GGA (blue) [30]. Figure taken from publication I. Copyright © 2022 by American Physical Society. All rights reserved.

final lifetimes are obtained as

$$\tau = \frac{1}{\Gamma_c^{DFT} + \Gamma_v^{QMC}}, \tag{4.21}$$

with the QMC-estimated valence and DFT-estimated core annihilation rates $\Gamma_c^{DFT}$ and $\Gamma_v^{QMC}$. Finally, the experimental lifetime values for the materials are shown.

We find that backflow-corrected wave functions (Sec. 2.3.5) improve the estimation of $g(0)$ when compared against experimental lifetimes. The lifetimes obtained with QMC for the set of test materials outperform the previous methods, demonstrating the importance of explicitly treating the interparticle correlations of the many-body wavefunctions when simulating positron annihilation.

We have not extrapolated the results to infinite system size, as this would require further studies on the dependence of $g(0)$ on finite-size effects. However, the results are not changing much when the system size is increased. The worst

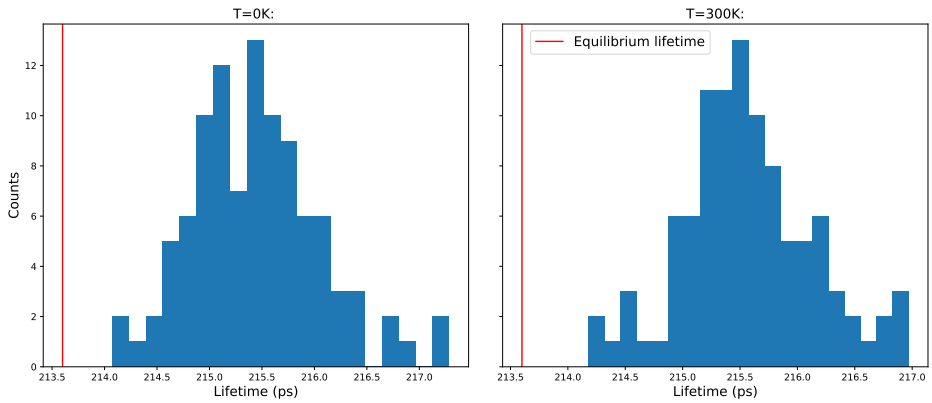


Figure 4.5: Lifetime results (blue histograms), obtained with DFT and BN-LDA, in a 64-atom cubic Si simulation cell from sampled set of atomic configurations distributed according to the vibrational modes in 0 and 300K. The horizontal red line shows the equilibrium lifetime. Figure taken from publication I. Copyright © 2022 by American Physical Society. All rights reserved.

correspondence with experiment in our QMC results is in Si, where DFT-based methods are more accurate than QMC. The reason is unknown, and will require further studies.

### 4.4.2 Effect of atomic vibrations on positron lifetimes in Si

Figure 4.5 shows lifetime results from DFT simulations with B15-GGA in a 64-atom Si simulation cell for a sampled set of atomic configurations distributed according to vibrational modes in 0 and 300K. The sets are sampled according to theory and algorithm explained in Sec. 3.4. The vertical red lines show the equilibrium lifetime. Fig. 4.5 reveals that on average the atomic vibrations increase the positron lifetime by 2 ps. However, fitting of a Gaussian distribution over the vibrational lifetime histograms gives a standard deviation of $\sim 1$ ps in the vibrational lifetimes. This, together with the statistical errorbar of $\sim 2$ ps in the QMC results in Fig. 4.4 means that based on the results at hand vibrations do not change the lifetimes in comparison with the equilibrium structure. Therefore the vibrational effects do not explain the discrepancy we have with experiments in the QMC results of positron lifetime in Si.

### 4.4.3 Doppler broadening of the annihilation radiation

As with positron lifetimes, in Publication II we have estimated Doppler spectra and tested finite-size convergence, necessity of backflow corrections and the effect of the treatment of the core electrons. Also the independence of Doppler spectra of the lattice vibrations in Si was verified. It was found that the results were converged already with cell sizes of 16 atoms in C, AlN, and Si. The use of

backflow did not change the results. Also the vibrational effects did not change the results. These observations provided the very promising notion on the low computational cost of Doppler spectra simulations with VMC also in vacancy systems that require larger simulation cells in theoretical calculations.

The Doppler broadening results from QMC simulations, as compared against experiments and DFT simulations within state-dependent and -independent models, are presented for AlN in Fig. 4.6 along direction $[\bar{1}2\bar{1}0]$. The bottom panel of the images presents the absolute error of the theory against experiment for the QMC and DFT estimates. The Monte Carlo errorbars, depicted in grey shaded regions around the QMC projections, were computed by calculating the Doppler projections for each twist vector separately and taking the standard deviation of the results. We can see that the QMC estimation is almost perfectly overlapping with experiment, demonstrating a clear improvement of the theoretical predictions when compared with DFT results.

In Publication II, theory-experiment comparison for Si are also presented, showing similar features as in AlN. These very accurate results, together with the relatively low computational costs of the APMD calculations with VMC, show great promise for VMC-supported Doppler broadening studies utilizing positron annihilation.

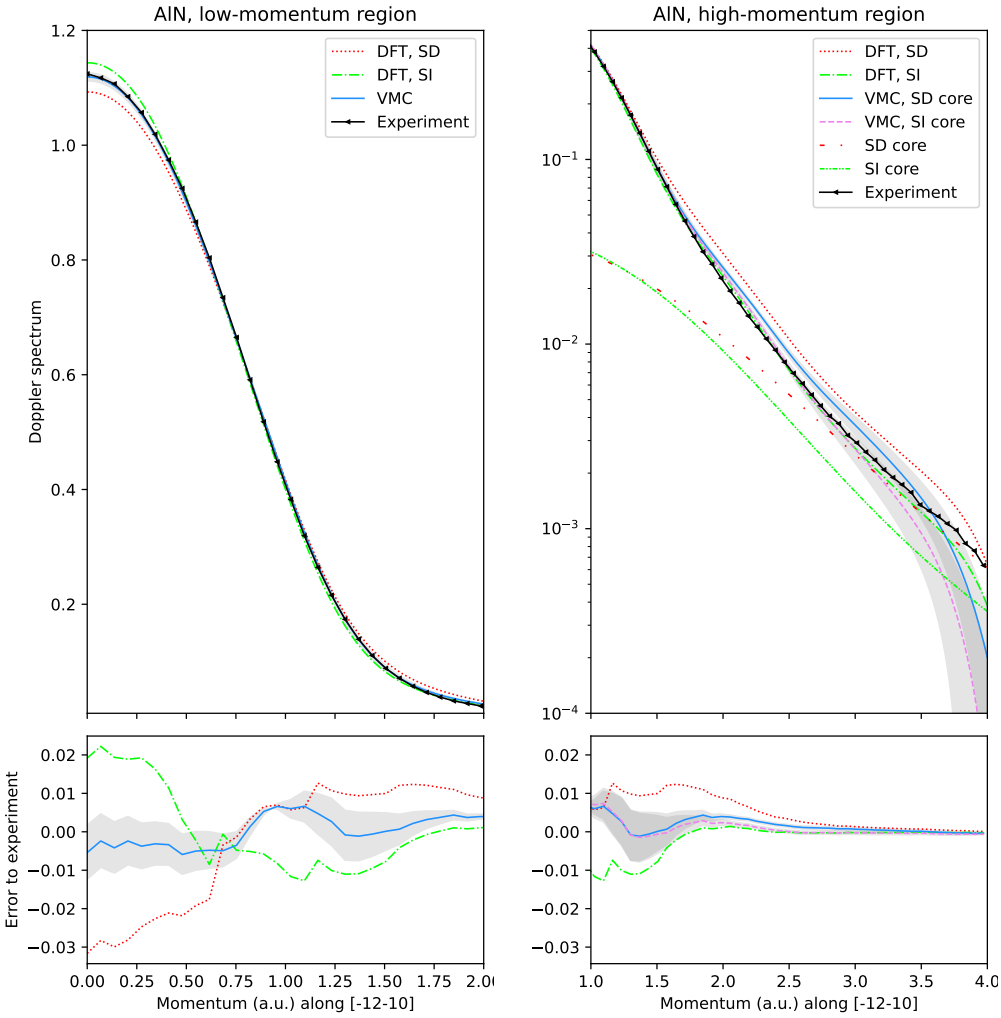


Figure 4.6: The low- and high-momentum parts (in left and right, respectively) of the AlN Doppler spectrum along the $[\bar{1}2\bar{1}0]$ direction. The data includes the experimental benchmark result [24] (black), our VMC data (blue, and violet when state-independent (SI) core spectrum is used), and for comparison the DFT-based results calculated by the state-dependent (SD, red) and state-independent (pink) models. The core spectrum obtained from these models and used also in QMC is shown separately. In the left, the state-dependent core spectrum was added to the QMC valence spectrum, in the right, QMC with both core spectra is shown. Copyright © 2023 by American Physical Society. All rights reserved.

# Chapter 5

# Vertical excitation energies of the $NV^-$-center in diamond

## 5.1 Overview

The NV center in diamond consists of a vacancy accompanied by a nitrogen atom at a nearest-neighbour site of the vacancy. It belongs to the class of solid state defects that have a non-zero ground state spin, which is initializable [41] and readable even at room temperature [39, 40]. The bulk solid surrounding the defects protects the spin states from external noise, which gives states long coherence times [37, 38]. Spin qubits formed of such solid-state defects have shown potential in quantum sensing [104], networks [105], and computing [46, 106, 107]. There are also point defect applications for single-photon emitters [108, 109] and quantum memory platforms [38, 110, 111]. The NV center in diamond was discovered early to have promising features for qubit operation, and due to large number of studies concerning the system since its discovery it has emerged as a testbed for new theoretical methods aiming to generalize the ability to study solid-state spin qubits. Of particular interest has been the negatively charged defect, the $NV^-$-center, which is the focus of this work, as it displays a spin-triplet ground state.

The electronic states have a strong many-body character in the $NV^-$-center [59]. The energy structure of these states is depicted in Fig. 5.1. According to this widely accepted picture of this system the ground state is a fully symmetric triplet state, labelled as $3A_2$. The state that is second lowest in energy is the doubly degenerate singlet $1E$ state, and above it lies the fully symmetric singlet $1A_1$ state. Above these three states there is the doubly degenerate triplet $3E$ state. The energy difference between the triplets is 2.19 eV in the ground-state structure, and the difference between the singlets is 1.19 eV [112–115]. The optical transitions that can be measured happen between the triplets or the singlets, and

triplet-to-singlet (or singlet-to-triplet) transitions happen via intersystem crossing [47].

Theoretically, the properties of interest in the $NV^-$-center include the energies of the excited states with respect to the ground state, atomic structures of the ground and excited states as well as the related Stokes and anti-Stokes shifts, the transition rates between the singlets and the triplets, the zero-field-splitting of the triplet states, the coupling of the lattice vibrations to different electronic states and the spin-orbit effects [47], to name a few. An *ab initio* method capable of predicting these properties for solid-state spin qubits in general would enable accelerated search of new spin qubits as well as improved ability to control the existing ones. Despite a variety of efforts [48–51, 59, 116–122], a general method able to tackle these problems with high predictive power is still missing.

DFT with hybrid HSE06 functional can estimate very accurate excitation energy and Stokes shifts for the triplet states with the so-called constrained DFT approach, where the occupation of the electronic orbitals is forced into a certain configuration corresponding either the ground or excited-state triplet [120]. Later work has shown how DFT can also be used to study spin-orbit effects and dynamical Jahn-Teller effects with simulation cell sizes up to thousands of atoms [121]. This is particularly important as the simulation cell sizes found to be convergent with respect to finite-size effects are found to consist of hundreds of atoms [120] for excitation energies and even thousands of atoms for spin-orbit effects [121]. A very recent work [122] has shown how DFT can also be applied to the singlet states that have multireference character [123]. A comparison of the vertical excitation energies in the $NV^-$-center from different theoretical methods is presented in Fig. 5.2.

Many-body methods that directly model the correlations have been more widely used to predict properties of the NV center than DFT. Most of these methods are taken from quantum chemistry, and their computational cost does not scale well against system size. Hence the methods often rely on atomic cluster models [48, 49] or embedding schemes [50–52], where the defect and the surrounding solid is first modelled with lower level of theory, such as DFT, and the resulting single-particle orbitals are then used to establish an embedded region for treatment with a more involved method. Time-dependent hybrid density functional theory has given fairly good results on the vertical excitation energies [119]. Complete active space multiconfiguration SCF [49] method in an atomic cluster has given also good results, but overestimate the singlet-to-singlet transition energy. Spin-flip Bethe-Salpeter equation approach [118] is a sophisticated recent implementation for modeling the excitation energies, but it underestimates the $1A_1$ singlet energy. GW approximation and BSE (GW+BSE) suffer from the same issue. One of the most successful method so far has been the so-called constrained random-phase approximation [117] that relies on an embedding scheme.

Because of the infavourable scaling with respect to system size, the many-body methods listed above rely usually on relatively small simulation cell or cluster

sizes. Embedding schemes can provide a way out of this, but they can suffer from issues of double counting, screening of the defect electrons by the bulk electrons, and the choice of the underlying DFT functional in treating the bulk [52]. This is where QMC, as implemented in e.g. DMC or auxiliary-field Monte Carlo approaches, can provide a way out: their favourable scaling of computational cost with respect to system size and the parallelizability of the QMC methods enable fully correlated studies of large simulation cell sizes, without cluster models or embedding schemes, so that we can calculate defect properties without free parameters. A possible extension in later studies could be QMC embedding, where the scaling of QMC with respect to systems size enables larger embedding clusters than so far has been possible.

In this work, DMC was used to calculate the vertical excitation energies of the NV$^-$-center in diamond in order to study the capability of the method to model the defect states. Previously, DMC has been used to compute defect formation and migration energies, [53–56], and also excitation energies in certain solid-state defects [53, 57, 58]. Only the study in Ref. [53] has used multideterminant wave functions, with fairly good success, in the simulation of the states in the monovacancy in diamond. This work uses larger simulation cell sizes than the previous works for the defect excitation energies, and to the knowledge of the author includes a backflow function for the first time in a DMC simulation of a solid-state defect. The study is an interesting test for the DMC method with backflow and small determinantal expansions: correlations of the states in the NV$^-$-center are strong, meaning that one would need large multideterminant expansions to capture the dynamic correlations, while fairly small expansions should suffice for static correlations. DMC is very powerful in capturing dynamic correlations, but it is not clear how well it can capture the static correlations. In case the small determinant expansions used in this work do not produce satisfactory results, the reason can be in the poor description of the static correlations. Of course DMC wave functions can be constructed very large amount of determinants, but currently this approach is limited to relatively small systems, as simultaneous extrapolation of results to both infinite system size and infinite amount of determinants is extremely challenging [7].

Besides presenting a new method for studying solid-state spin qubits, this work has another motivation in extending the simulation of positrons to solid-state defects in general. A successfull simulation of the highly correlated states of the NV center would mean that DMC is capable of capturing the electronic correlations in this system, suggesting that the methods developed for positron annihilation studies in this work could be directly taken into use in the study of positrons trapped at open-volume defects.

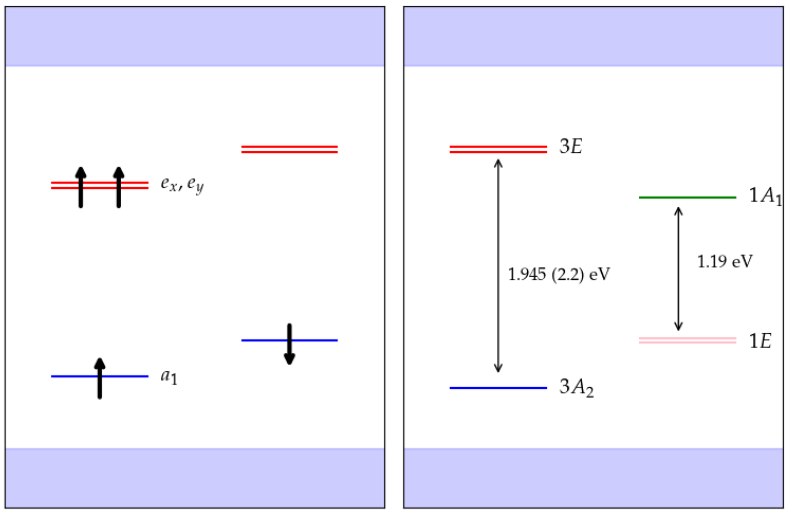


Figure 5.1: Sketch of the energy structure of the single-particle orbitals (left) and the many-body states (right) of the $NV^-$-center. A gap between the spin channels of the single-particle orbitals is shown, so that the spin-majority (spin-up) channel in the left has orbitals with lower energies than the spin-minority (spin-down) channel. The electronic occupation of the single-particle orbitals in the $3A_2$ ground state is denoted for spin-up (upward arrow) and spin-down (downward arrow) electrons. The many-body states in energetic order from lowest to highest energy are 3A2 (blue), 1E (pink), $1A_1$ (green), and 3E (red). The double arrows denote the triplet-to-triplet and singlet-to-singlet transitions, with experimental values shown in eV. The energies of the doubly degenerate orbitals $e_{x,y}$ and the many-body states $3E$ and $1E$ are represented with two lines, displaced vertically for easier depiction. Copyright © 2022 by American Physical Society. All rights reserved.

## 5.2 Modeling the electronic states

### 5.2.1 Constructing the wave functions for the $NV^-$-center

The construction of wave functions for the solid state defects can be done with the molecular orbital method [124–126]. The method considers the atoms in the lattice to be covalently bonded and makes the assumption that the wave function of the defect in the immediate surroundings of the defect are completely determined by the dangling bond states that are formed when the vacancy is introduced into the system. The electrons on these states are assumed to be localized around the defect site.

The many-body wave functions for the defect states can be built out of the dangling bond electrons with a symmetry projection method, that is derived from group theory [127]. The dangling bonds of the nearest-neighbour carbon atoms of the NV center, $\sigma_1, \sigma_2$, and $\sigma_3$, and the dangling bond of the nitrogen atom, $\sigma_N$, constitute a basis for expressing the single-particle orbitals of the defect. We can define a single-particle Hamiltonian $\hat{H}_0^i$ for any single electron in the dangling bond basis, which is subject to the same symmetries as the atomic structure of

| $E$ | $C_3^+$ | $C_3^-$ |
|---|---|---|
| $\begin{pmatrix}1&0&0&0\\0&1&0&0\\0&0&1&0\\0&0&0&1\end{pmatrix}$ | $\begin{pmatrix}0&0&1&0\\1&0&0&0\\0&1&0&0\\0&0&0&1\end{pmatrix}$ | $\begin{pmatrix}0&1&0&0\\0&0&1&0\\1&0&0&0\\0&0&0&1\end{pmatrix}$ |

| $\sigma_d$ | $\sigma_e$ | $\sigma_f$ |
|---|---|---|
| $\begin{pmatrix}1&0&0&0\\0&0&1&0\\0&1&0&0\\0&0&0&1\end{pmatrix}$ | $\begin{pmatrix}0&0&1&0\\0&1&0&0\\1&0&0&0\\0&0&0&1\end{pmatrix}$ | $\begin{pmatrix}0&1&0&0\\1&0&0&0\\0&0&1&0\\0&0&0&1\end{pmatrix}$ |

Table 5.1: The symmetry matrices of the $C_{3v}$ point group in the dangling bond basis for the NV$^-$-center. The top row from left to right shows the matrices for identity, clockwise $2\pi/3$, and anti-clockwise $2\pi/3$ symmetry operations. The bottom row shows the reflections with respect to three planes of symmetry.

the defect. The relevant symmetry group is $C_{3v}$. Since the symmetry operations leave the Hamiltonian invariant, the symmetry operations and the Hamiltonian commute and have therefore the same eigenstates. Thus, instead of solving the Schrödinger equation for $\hat{H}_0^i$, we can project out of the dangling bond basis the states that transform according to the irreducible representations of $C_{3v}$, which are also the eigenstates of $\hat{H}_0^i$, i.e. the single-particle orbitals. The projection is done by applying the group-theoretic projection operator,

$$\mathbf{P}^\alpha = \frac{n_\alpha}{\lambda_{C_{3v}}} \sum_{g \in C_{3v}} \chi^{(\alpha)*}(g) \Gamma^\sigma_{C_{3v}}(g), \tag{5.1}$$

to the dangling bonds. Above, $n_\alpha$ is the dimension of the irreducible representation $\alpha$, $\lambda_{C_{3v}}$ is the number of elements in $C_{3v}$, $\Gamma^\sigma_{C_{3v}}(g)$ is a representation of symmetry operation $g \in C_{3v}$ in the dangling bond basis, and $\chi^{(\alpha)}(g)$ is the character, i.e. the trace of the irreducible representation $\alpha$ of the symmetry operation $g$. The symmetry operations of $C_{3v}$ in the dangling bond basis $(\sigma_1, \sigma_2, \sigma_3, \sigma_N)$ are presented in Table 5.1 and the corresponding characters in Table 5.2. The projection leads to 4 single-particle orbitals:

$$\begin{aligned} a_N &= \sigma_4 \\ a_1 &= [\ \sigma_1 + \sigma_2 + \sigma_3]/3 \\ e_x &= [2\sigma_1 - \sigma_2 - \sigma_3]/\sqrt{6} \\ e_y &= [\qquad \sigma_2 - \sigma_3]/\sqrt{2}. \end{aligned} \tag{5.2}$$

DFT simulations give 3 orbitals in the band gap of diamond in a simulation cell including a $NV^-$ center. Based on the shapes of the orbitals and group-theoretic energy considerations [126] we know that these three orbitals consist of $a_1$ that lies lower in energy and $e_x$ and $e_y$ that are degenerate and lie higher in energy. The

| $C_{3v}$ | $E$ | $2C_3$ | $3\Lambda$ |
|---|---|---|---|
| $A_1$ | 1 | 1 | 1 |
| $A_2$ | 1 | 1 | $-1$ |
| $E$ | 2 | $-1$ | 0 |
| $\Gamma^\sigma$ | 4 | 1 | 2 |

Table 5.2: The character table of the irreducible representations ($A_1$,$A_2$,$E$) and the representation in the dangling bond basis ($\Gamma^\sigma$, see Table 5.1) of the symmetry group of the single-particle Hamiltonian of the $NV^-$-center. The columns represent the symmetry classes: identity ($E$), two $\pm 2\pi/3$ rotations ($C_3$) and 3 reflections $\Lambda$.

$a_N$ orbital lies below the valence band and is assumed to always be fully occupied. Therefore, with 6 electrons attached to the $NV^-$-center – three originating from the nearest-neighbour carbon atoms, two from the nitrogen atom and one from nitrogen donors in the diamond lattice – there are 4 electrons occupying the band gap states. The many-body-states built out of these states have the same analytic features as diradical molecules, that have been considered in earlier research with QMC methods [128, 129]. A sketch of the energetics of the single-particle orbitals is presented in Fig. 5.1.

The set of Slater determinants that can be formed by occupying the band gap states with 4 electrons are eigenstates of $\hat{H}_0 = \sum_{i=1}^{N} \hat{H}_0^i$, where $N$ is the number of electrons in a given simulation cell. A representation of the symmetry group of $\hat{H}_0$ can be chosen to consist of all of the tensor products of the form $\Gamma^\sigma_{C_{3v}}(g_1) \otimes \Gamma^\sigma_{C_{3v}}(g_2) \otimes ... \otimes \Gamma^\sigma_{C_{3v}}(g_N)$, where $g_i$ is any symmetry operation in $C_{3v}$ acting on electron $i$. The symmetry group of the full Hamiltonian $\hat{H}$ that consists of also the Coulomb interactions between the electrons can have a representation of its symmetry group with the same tensor product form, but with the restriction $g_1 = g_2 = ... = g_N$. This is obvious: the Coulombic interaction term of the full Hamiltonian remains invariant under simultaneous rotation of all of the particles only if all the particles undergo the same rotation. The restriction makes the symmetry group of $\hat{H}$ a subgroup of $\hat{H}_0$ and isomorphic with the group of $\hat{H}_0^i$ [130].

We can project the Slater determinants formed by occupying the band gap single-particle states with 4 electrons into states that transform according to irreducible representations of the symmetry group of $\hat{H}$ with a projection operator similar to that in Eq. (5.1), but with the symmetry representations replaced by the appropriate tensor products and using the corresponding characters. This results

in the following many-body wave functions:

$$
\begin{aligned}
&\mathbf{a^2e^2}: \\
&3A_2 = \begin{cases} m_s = 1 : D^{\uparrow}(e_x e_y) D^{\downarrow}(a) \\ m_s = 0 : D^{\uparrow}(a e_x) D^{\downarrow}(a e_y) - D^{\uparrow}(a e_y) D^{\downarrow}(a e_x) \\ m_s = -1 : D^{\uparrow}(a) D^{\downarrow}(a e_x e_y) \end{cases} \\
&1E = \begin{cases} x : D^{\uparrow}(a e_x) D^{\downarrow}(a e_y) + D^{\uparrow}(a e_y) D^{\downarrow}(a e_x) \\ y : D^{\uparrow}(a e_x) D^{\downarrow}(a e_x) - D^{\uparrow}(a e_y) D^{\downarrow}(a e_y) \end{cases} \\
&1A1 = D^{\uparrow}(a e_x) D^{\downarrow}(a e_x) + D^{\uparrow}(a e_y) D^{\downarrow}(a e_y) \\
&\mathbf{ae^3}: \\
&3E = \begin{cases} x, m_s = 1 : D^{\uparrow}(a e_x e_y) D^{\downarrow}(e_x) \\ y, m_s = 1 : D^{\uparrow}(a e_x e_y) D^{\downarrow}(e_y) \\ x, m_s = 0 : D^{\uparrow}(e_x e_y) D^{\downarrow}(a e_x) - D^{\uparrow}(a e_x) D^{\downarrow}(e_x e_y) \\ y, m_s = 0 : D^{\uparrow}(e_x e_y) D^{\downarrow}(a e_y) - D^{\uparrow}(a e_y) D^{\downarrow}(e_x e_y) \\ x, m_s = -1 : D^{\uparrow}(e_x) D^{\downarrow}(a e_x e_y) \\ y, m_s = -1 : D^{\uparrow}(e_y) D^{\downarrow}(a e_x e_y) \end{cases} \\
&1E' = \begin{cases} x : D^{\uparrow}(a e_x) D^{\downarrow}(e_x e_y) + D^{\uparrow}(e_x e_y) D^{\downarrow}(a e_y) \\ y : D^{\uparrow}(a e_y) D^{\downarrow}(e_x e_y) - D^{\uparrow}(e_x e_y) D^{\downarrow}(a e_y) \end{cases} \\
&\mathbf{e^4}: \\
&1A1' = D^{\uparrow}(e_x e_y) D^{\downarrow}(e_x e_y),
\end{aligned}
\tag{5.3}
$$

where the spin-up and -down determinants $D^{\uparrow}$ and $D^{\downarrow}$ are denoted by the occupied single-particle orbitals in the band gap. $\mathbf{a^2e^2}$ and $\mathbf{a^2e^2}$ are categorization denotions referring to the amount of electrons occupying the $a$- and $e$-orbitals in the band gap. The $1E'$ and $1A1'$ states lie higher in energy than the others that were mentioned before, and are not considered in this work.

### 5.2.2 Variational principle for excitation energies with diffusion Monte Carlo

The DMC method that is used to estimate the energies of the many-body states of the NV$^-$-center is devised for the description of the ground state wave function. However, DMC can be also used to study excitations. When simulating excited states, the variational principle applies only for states transforming according to 1-dimensional irreducible representations of the symmetry group of the many-body Hamiltonian [131]. States transforming according to irreducible representation of higher dimension can also have variational principle, or a weaker variational principle, but this must be studied separately. Publication III of this thesis inspects the applicability of the variational principles to the excited states of the NV center, and shows that a strong variational principle also applies to the degenerate $1E$ and $3E$ states.

If the variational principle does not apply for the excited states, the nodal surface error can cause the energy estimate of the excited state to be lower than the actual energy. In this case the computed vertical excitation energy is an underestimation. The bias in energy is due to nodal surface errors is larger without variational principle. Also, the nodal surface errors of the excitations are expected to be larger even when the variational principle applies. Hence the excited states must be carefully optimized for minimal nodal surface errors.

### 5.2.3 Nodal surface errors

The DMC energy projected out of the trial wave function is biased by the fixed node error. An obvious way to improve this error is to increase the amount of Slater determinants used in representing the many-body states to push the wave function towards the full solution as in Eq. (2.12), but this can quickly lead to impractically large computational expenses. Instead, in Publication III the nodal surface errors are minimized in several ways. First, the DFT correlation functional used to prepare the single-particle orbitals that construct the Slater determinants are sought for minimal energy. HSE06 correlation functional [132] turned to give lowest energies when used in finding the single-particle orbitals in comparison to PBE and HF methods. Second, for the highly correlated singlet states $1E$ and $1A1$ it is inspected whether inclusion of their coupling to the higher lying $1E'$ and $1A1'$ states of same symmetry to the simulated wave functions improve the energy. Including higher-lying states is equal to adding determinants to the trial wave functions, changing the nodal surface. Finally, the use of backflow function is inspected, and it is found to improve the excitation energies.

### 5.2.4 Spin contamination

As mentioned already in this thesis, QMC with Slater-Jastrow wave functions can currently only treat systems without explicitly including spin dependence to the wave functions. Hence the wave functions used to describe the states of the NV center are not eigenstates of the total spin of the system. The wave functions, although properly containing spatial symmetries of the many-body states, might contain components of other states with the same total spin. Inconsistencies in the treatment of spin channels in the Jastrow factor or the backflow function, or in the generation of the single-particle orbitals, are potential sources of spin contamination, causing bias in the simulation. Also the $m_s = 0$-components (see Eq. (5.3)) of the triplet states are not quaranteed to be properly projected out of the trial wave functions by the DMC algorithm, as DMC targets to the lowest state of a given spatial symmetry only, and might project out a triplet state contaminated by higher lying singlets.

In Publication III, the spin contamination is studied by computing the energies of all of the spin components of the triplets and by varying the method used to pro-

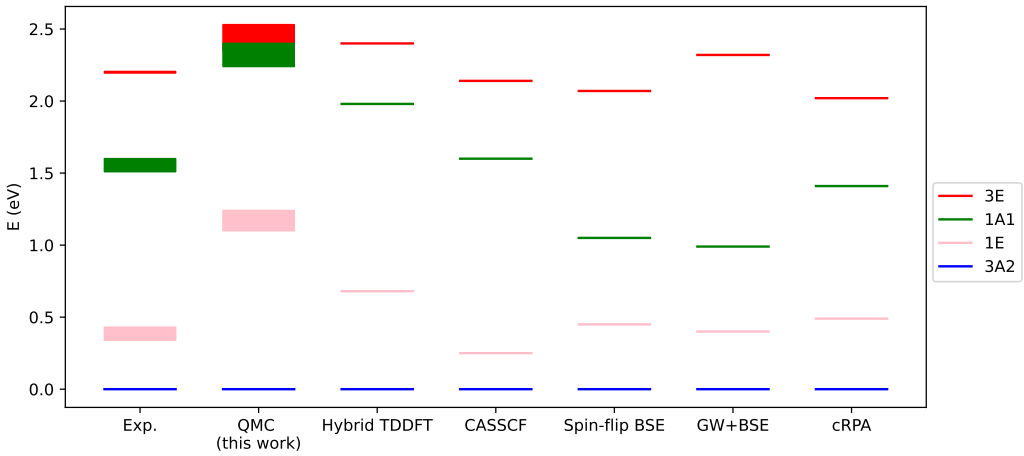


Figure 5.2: Vertical excitation energies from experiments [112–115] and QMC (this work), compared against results from a number of theoretical methods: hybrid time-dependent DFT (hybrid TDDFT) [119], complete active space multiconfiguration SCF (CASSCF) [49], spin-flip Bethe-Salpeter equation approach (Spin-flip BSE) [118], GW approximation and BSE (GW+BSE) [116], and constrained random-phase approximation (cRPA) [117]. Copyright © 2022 by American Physical Society. All rights reserved.

duce the single-particle orbitals; we either choose spin-restricted or -unrestricted DFT simulation in generating the orbitals. Spin-restricted calculation is shown to be very important for the singlet states, while spin-unrestricted calculation gives lower energies when simulating the triplets.

### 5.2.5 Finite-size errors

As in any periodic simulation, in computing the energies of the many-body states of the NV⁻-center we must study the finite-size effects. To do this, we use two simulation cells in the studies of the NV⁻-center: cubic 63- and 215-atom simulation cells, and extrapolate the DMC energies to infinite system size. Also a 511-atom cell was used when the structural relaxation was studied to check the convergence of the atomic relaxation with respect to system size.

Previous results using DFT and other methods have paid great deal of attention to the study of the finite-size effects in the energies of the NV center. Using these results and DFT simulations in cells up to 511 atoms in this study the different sources of the finite-size effects can be analysed and extrapolation scheme can be established. In Publication III, a more detailed consideration is given to these issues.

## 5.3 Results

Figure 5.2 shows the QMC results for the vertical excitations of the $NV^-$-center against experimental estimates [112–115] and previous theoretical values [49, 116–119]. The ground- and excited-state energies were evaluated in the ground state structure that was optimized using DFT and HSE06 hybrid functional. It can be seen that, while QMC is comparable to the other methods in accuracy, its energies for the excited states are overestimations against experiment. However, the singlet-to-singlet transition is very accurate, comparable in accuracy to best results for this observable from previous theoretical studies. Also the triplet-to-triplet transition has a relatively good result, with a slight overestimation of $\sim 300$ meV.

As we have studied the finite-size effects, use of different pseudopotentials, DMC time step errors, and the correct choice of orbitals for constructing the Slater determinant (see Publication III), the most probable reason for the overestimation is nodal surface error. The backflow improves the values, but it is uncertain how well the backflow can describe the strong static correlations present in the many-body states [59]. Thus, to improve the current results a study with larger multideterminant expansion in DMC should be done.

Because the triplet-to-triplet and singlet-to-singlet transition energies are relatively accurate, the nodal surface errors are probably cancelled in the transition energies. Also because the amount of spin contamination in singlet and triplet states has not been estimated, the energy differences between triplets and singlets are not as well defined as the differences between the states of the same spin multiplicity. Thus the accurate results for the $3A2 \rightarrow 3E$ and $1E \rightarrow 1A1$ transitions hint that at least for states of the same spin multiplicity the excitation energies are relatively well estimated by DMC with backflow.

The results, although overestimations, have demonstrated DMC's capability to capture the essential features of the NV center that make it interesting in quantum technology. DMC has been used in very large simulation cells compared to what is reachable for most quantum chemistry methods, providing means to study finite-size effects with a fully correlated method. Because the wave functions are variational, systematic improvement of the wave functions used is possible. Hence DMC is a viable method for future solid-state spin qubit studies. Also, the current results hint that simulation of positrons in lattice defects with multireference character in electronic structure is possible, but should be tested before making conclusions. In other defect systems [53, 57, 58], DMC's ability to capture excitation energies has been even better, Meaning that the electronic structure is better captured. DMC is best at describing ground states, and the positrons are mainly interacting with the electronic ground states of the defects, so probably positron studies in defects in general is viable with the computational machinery established in this thesis.

# Chapter 6

# Summary

This thesis presents calculations of measurable positron annihilation parameters in crystalline matter and optical transitions in the $NV^-$-center of diamond with quantum Monte Carlo methods. The work has required theoretical and computational studies of the phenomena, but also a significant proportion of the time has been consumed in developing and testing new computational applications. Especially the methods related to positron studies has required development of new algorithms and extensions of the existing ones. Hence this thesis represents only part of the work required to obtain the results presented in the Publications.

Publications I and II on the positron annihilation parameters in C, AlN, Si and Li present the calculations and results obtained by using the theory introduced so far. The results, when compared with earlier state-of-the-art theory and experiments, show that both the positron lifetime and the Doppler broadening of the annihilation radiation can be more accurately predicted with the methods developed in this work. The main improvement to existing theory has been the simulation of positron interactions with the surrounding system of solid-state matter with the long-range correlations included. This is unprecedented to date as the previously existing methods have been relying on approaches such as DFT.

The results in the Publications I and II work as a validation of the method presented in this work. Now it is known that QMC can be used to tackle current problems of physics of positrons in solids. Further work will should establish a pool of results for the positron annihilation parameters in theoretically and technologically relevant materials, which can help in studying and developing existing theory as well as in supporting experimental studies. Another issue where the methods of this work can be immediately taken into use are materials where the bulk lifetime and Doppler broadening are not known, because defect-free samples are not available, making the experimental positron studies of e.g. gallium oxide very problematic [133]. Reliable theoretical modeling of positron states in $Ga_2O_3$ and other problematic materials would be a valuable asset for experimental studies.

Importantly, the modeling of positron states in lattice defects with quantum Monte Carlo has not been done yet. This is an extremely complicated task because of both computational requirements and theoretical considerations. The developed QMC methods for the estimation of positron annihilation parameters should work as such for lattice defect studies, but the nature of trapped positron states is very different, as are the electronic states relevant for annihilation, as they are now localized around the defect. Also the electron density in the vicinity of the positron trapped into a vacancy is lower. Hence, a system of positron trapped into a lattice defect is more strongly correlated than bulk systems with delocalized positrons. Furthermore, problems related to the structural relaxation of the defect have to be taken into account, so that also the effect of the positron to the atomic structure is correctly treated. Publication III in this work tackles the problem of modeling the electronic states of the $NV^-$-center in diamond with QMC. This is an inherently many-body problem, as the singlet states cannot be modeled with independent particle theories due to their multideterminant nature. Because of its technological relevance, the many-body states and the related optical transitions and energy differences have been studied extensively both theoretically and experimentally with methods other than diffusion Monte Carlo. This makes the $NV^-$-center an ideal system to test QMC modeling of electronic states bound to lattice defects, and the results can be benchmarked against existing results. Publication III shows that QMC is able to capture the correlations of the electronic states, as the vertical excitation energies between the ground and excited states are comparable against earlier theory and experiments.

The results on the $NV^-$-center have two implications. First, based on DMC's capability to capture some of the essential features of the many-body structure of the $NV^-$-center, QMC methods for studies of magneto-optical properties of lattice defects could be used for studies of new solid-state spin qubits. Second, the work justifies further developments of QMC for lattice defect studies. One is the extension of the Hamiltonian to include spin terms. This would allow better definition of the different spin states and avoid the problem of spin contamination. Also it would give access to the important spin-orbit and zero field splitting effects. Another is the development of embedding schemes, used widely with quantum chemistry algorithms but still rare for QMC. Because of the favourable scaling in required computational resources with respect to both system size and computational power, QMC embedding could be used with very large volumes treated with explicit correlations. There are also issues of structural relaxation with explicitly correlated methods and the inclusion of vibrational effects into the simulations. There are thus many systems for further studies and many fields requiring development of new algorithms.

Another implication of the work on the $NV^-$-center is that it gives the framework for studies of positrons in lattice defects with QMC. Hence the only remaining ingredient for the method of many-body simulation of positrons in solids is immediately within reach. Therefore the Publications in this study, when taken

together, directly show how the powerful method of quantum Monte Carlo can be applied to support all fields of experimental positron physics in solid-state matter.

# Acknowledgements

The plan for the development of a quantum Monte Carlo simulation tool for positron simulations in solids was originally designed by the supervisor of my doctoral studies, Dr. Ilja Makkonen. As the work presented in this Thesis shows, these ideas have provided valuable contributions in the field of positron physics. I am thankful to Ilja for trusting me with the completion of this project, which has been a challenging but rewarding experience, helping me develop crucial research skills and expand my knowledge across various disciplines. I also want to thank Ilja for his support throughout the work, as his expertise has been very important in overcoming obstacles and shaping my understanding of computational physics. Additionally, I appreciate the freedom he provided me to explore new ideas without strict deadlines.

Crucial contributions and support to this project was also provided by Dr. Neil Drummond from Lancaster University. As a quantum Monte Carlo expert with experience of positron studies, Neil showed us theoretically sound and practically efficient ways to implement and test the positron simulation tools with the CASINO package. Despite the physical distance between us, Neil has always been available to offer instructions, opinions, and contributions to our work, enabling the current quality of the Thesis. Neil has also been a great host during my two visits to Lancaster, and I am very happy to have had such a great collaborator during this work.

Professor Filip Tuomisto has created pleasant working conditions and atmosphere first in his group in Aalto University, where I started work on my doctoral thesis, and then in Helsinki Accelerator Laboratory. Although our research areas did not overlap as much as with Ilja and Neil, Filip has provided useful advice and comments on various issues. Working under his guidance has been enjoyable and relaxed.

I want to also thank various people in the positron laboratories both in Aalto and the accelerator laboratory for help on various issues in the beginning of my studies, and for the company during the work.

I am also grateful for the fundings from Jenny and Antti Wihurin rahasto and Suomen Kulttuurirahasto that have enabled me to finish my work.

Importantly, I have been fortunate to obtain generous computational resources

provided by CSC IT Center for Science LTD. Most of the computations in this work have been run first in Sisu and Taito, then in Mahti, Puhti and Lumi supercomputers. I was also granted an important allocation of computing resources for ARCHER National Supercomputing Service, UK, by PRACE (Partnership for Advanced Computing in Europe) TIER-1 DECI access.

-

# Bibliography


[1] P. A. M. Dirac, Proceedings of the Royal Society of London. Series A, Containing Papers of a Mathematical and Physical Character **123**, 714 (1929).

[2] P. Hohenberg and W. Kohn, Phys. Rev. **136**, B864 (1964).

[3] W. Kohn and L. J. Sham, Phys. Rev. **140**, A1133 (1965).

[4] R. M. Martin, *Electronic structure: basic theory and practical methods* (Cambridge university press, 2020).

[5] W. M. C. Foulkes, L. Mitas, R. J. Needs, and G. Rajagopal, Rev. Mod. Phys. **73**, 33 (2001).

[6] N. Metropolis, A. W. Rosenbluth, M. N. Rosenbluth, A. H. Teller, and E. Teller, J. Chem. Phys. **21**, 1087 (1953).

[7] R. Needs, M. Towler, N. Drummond, P. Lopez Rios, and J. Trail, J. Chem. Phys. **152**, 154106 (2020).

[8] W. Al-Saidi, S. Zhang, and H. Krakauer, J. Chem. Phys. **124**, 224101 (2006).

[9] J. Carlson, S. Gandolfi, K. E. Schmidt, and S. Zhang, Phys. Rev. A **84**, 061602 (2011).

[10] J. Shee, J. L. Weber, D. R. Reichman, R. A. Friesner, and S. Zhang, J. Chem. Phys. **158**, 140901 (2023).

[11] M. Troyer and U.-J. Wiese, Phys. Rev. Lett. **94**, 170201 (2005).

[12] G. H. Booth, A. J. Thom, and A. Alavi, J. Chem. Phys. **131**, 054106 (2009).

[13] G. F. Gribakin, J. A. Young, and C. M. Surko, Rev. Mod. Phys. **82**, 2557 (2010).

[14] F. Tuomisto and I. Makkonen, Rev. Mod. Phys. **85**, 1583 (2013).

[15] A. Charman, Nat. Commun. **4**, 1785 (2013).

[16] R. Wahl and J. Buchanan, Principles and Practice of Positron Emission Tomography (Lippincott, Williams and Wilkins, Philadelphia, PA, 2002) (2002).

[17] D. Schödlbauer, G. Kögel, P. Sperr, and W. Triftshäuser, Phys. Status Solidi (a) **102**, 549 (1987).

[18] R. Krause-Rehberg and H. S. Leipner, *Positron annihilation in semiconductors: defect studies*, vol. 127 (Springer Science & Business Media, 1999).

[19] R. A. Pethrick, Prog. Polym. Sci. **22**, 1 (1997).

[20] D. Gidley, W. Frieze, T. Dull, J. Sun, A. Yee, C. Nguyen, and D. Yoon, Appl. Phys. Lett. **76**, 1282 (2000).

[21] A. David, G. Kögel, P. Sperr, and W. Triftshäuser, Phys. Rev. Lett. **87**, 067402 (2001).

[22] G. Kontrym-Sznajd, Low Temp. Phys. **35**, 599 (2009).

[23] N. Segercrantz, J. Slotte, F. Tuomisto, K. Mizohata, and J. Räisänen, Phys. Rev. B **95**, 184103 (2017).

[24] J.-M. Mäki, F. Tuomisto, A. Varpula, D. Fisher, R. U. A. Khan, and P. M. Martineau, Phys. Rev. Lett. **107**, 217403 (2011).

[25] B. Chakraborty, Phys. Rev. B **24**, 7423 (1981).

[26] B. Chakraborty and R. W. Siegel, Phys. Rev. B **27**, 4535 (1983).

[27] R. M. Nieminen, E. Boronski, and L. J. Lantto, Phys. Rev. B **32**, 1377 (1985).

[28] E. Boroński and R. M. Nieminen, Phys. Rev. B **34**, 3820 (1986).

[29] B. Barbiellini, M. J. Puska, T. Torsti, and R. M. Nieminen, Phys. Rev. B **51**, 7341 (1995).

[30] J. Kuriplach and B. Barbiellini, Phys. Rev. B **89**, 155111 (2014).

[31] B. Barbiellini and J. Kuriplach, Phys. Rev. Lett. **114**, 147401 (2015).

[32] J. Hofierka, B. Cunningham, C. M. Rawlins, C. H. Patterson, and D. G. Green, Nature **606**, 688 (2022).

[33] V. Callewaert, R. Saniz, B. Barbiellini, A. Bansil, and B. Partoens, Phys. Rev. B **96**, 085135 (2017).

[34] W. Shi, V. Callewaert, B. Barbiellini, R. Saniz, M. Butterling, W. Egger, M. Dickmann, C. Hugenschmidt, B. Shakeri, R. W. Meulenberg, et al., Phys. Rev. Lett. **121**, 057401 (2018).

[35] Q. Yang, Z. Hu, I. Makkonen, P. Desgardin, W. Egger, M.-F. Barthe, and P. Olsson, J. Nuc. Mat. **571**, 154019 (2022).

[36] N. D. Drummond, P. López Ríos, R. J. Needs, and C. J. Pickard, Phys. Rev. Lett. **107**, 207402 (2011).

[37] H. Seo, A. L. Falk, P. V. Klimov, K. C. Miao, G. Galli, and D. D. Awschalom, Nat. Commun. **7**, 1 (2016).

[38] C. E. Bradley, J. Randall, M. H. Abobeih, R. Berrevoets, M. Degen, M. A. Bakker, M. Markham, D. Twitchen, and T. H. Taminiau, Phys. Rev. X **9**, 031045 (2019).

[39] M. G. Dutt, L. Childress, L. Jiang, E. Togan, J. Maze, F. Jelezko, A. Zibrov, P. Hemmer, and M. Lukin, Science **316**, 1312 (2007).

[40] W. F. Koehl, B. B. Buckley, F. J. Heremans, G. Calusine, and D. D. Awschalom, Nature **479**, 84 (2011).

[41] M. W. Doherty, N. B. Manson, P. Delaney, F. Jelezko, J. Wrachtrup, and L. C. Hollenberg, Phys. Rep. **528**, 1 (2013).

[42] S. S. Hegde, J. Zhang, and D. Suter, Phys. Rev. Lett. **124**, 220501 (2020).

[43] P. Siyushev, M. Nesladek, E. Bourgeois, M. Gulka, J. Hruby, T. Yamamoto, M. Trupke, T. Teraji, J. Isoya, and F. Jelezko, Science **363**, 728 (2019).

[44] L. Childress, M. Gurudev Dutt, J. Taylor, A. Zibrov, F. Jelezko, J. Wrachtrup, P. Hemmer, and M. Lukin, Science **314**, 281 (2006).

[45] G. Waldherr, Y. Wang, S. Zaiser, M. Jamali, T. Schulte-Herbrüggen, H. Abe, T. Ohshima, J. Isoya, J. Du, P. Neumann, et al., Nature **506**, 204 (2014).

[46] J. Zhang, S. S. Hegde, and D. Suter, Phys. Rev. Lett. **125**, 030501 (2020).

[47] Á. Gali, Nanophotonics **8**, 1907 (2019).

[48] P. Delaney, J. C. Greer, and J. A. Larsson, Nano Lett. **10**, 610 (2010).

[49] C. Bhandari, A. L. Wysocki, S. E. Economou, P. Dev, and K. Park, Phys. Rev. B **103**, 014115 (2021).

[50] Q. Sun and G. K.-L. Chan, Acc. Chem. Res. **49**, 2705 (2016).

[51] H. Ma, N. Sheng, M. Govoni, and G. Galli, J. Chem. Theory Comput. **17**, 2116 (2021).

[52] L. Muechler, D. I. Badrtdinov, A. Hampel, J. Cano, M. Rösner, and C. E. Dreyer, Phys. Rev. B **105**, 235104 (2022).

[53] R. Q. Hood, P. R. C. Kent, R. J. Needs, and P. R. Briddon, Phys. Rev. Lett. **91**, 076403 (2003).

[54] D. Alfe and M. Gillan, Phys. Rev. B **71**, 220101 (2005).

[55] W. D. Parker, J. W. Wilkins, and R. G. Hennig, Phys. Status Solidi B **248**, 267 (2011).

[56] R. Q. Hood, P. R. C. Kent, and F. A. Reboredo, Phys. Rev. B **85**, 134109 (2012).

[57] E. Ertekin, L. K. Wagner, and J. C. Grossman, Phys. Rev. B **87**, 155210 (2013).

[58] K. Saritas, W. Ming, M.-H. Du, and F. A. Reboredo, J. Phys. Chem. Lett. **10**, 67 (2018).

[59] Y. Chen, T. Jiang, H. Chen, E. Han, A. Alavi, K. Yu, E.-G. Wang, and J. Chen, arXiv preprint arXiv:2302.13730 (2023).

[60] V. Fock, Zeitschrift für Physik **61**, 126 (1930).

[61] J. C. Slater, Phys. Rev. **36**, 57 (1930).

[62] R. Jastrow, Phys. Rev. **98**, 1479 (1955).

[63] G. Rajagopal, R. J. Needs, S. Kenny, W. M. C. Foulkes, and A. James, Phys. Rev. Lett. **73**, 1959 (1994).

[64] G. Rajagopal, R. J. Needs, A. James, S. D. Kenny, and W. M. C. Foulkes, Phys. Rev. B **51**, 10591 (1995).

[65] A. Malatesta, S. Fahy, and G. B. Bachelet, Phys. Rev. B **56**, 12201 (1997).

[66] N. D. Drummond, M. D. Towler, and R. Needs, Phys. Rev. B **70**, 235119 (2004).

[67] T. Kato, Commun. Pure Appl. Math. **10**, 151 (1957).

[68] R. T. Pack and W. B. Brown, J. Chem. Phys. **45**, 556 (1966).

[69] C.-J. Huang, C. Filippi, and C. Umrigar, J. Chem. Phys. **108**, 8838 (1998).

[70] Y. Kwon, D. M. Ceperley, and R. M. Martin, Phys. Rev. B **48**, 12037 (1993).

[71] P. López Ríos, A. Ma, N. D. Drummond, M. D. Towler, and R. J. Needs, Phys. Rev. E **74**, 066701 (2006).

[72] R. P. Feynman and M. Cohen, Phys. Rev. **102**, 1189 (1956).

[73] N. D. Drummond, R. J. Needs, A. Sorouri, and W. M. C. Foulkes, Phys. Rev. B **78**, 125106 (2008).

[74] C. Lin, F. H. Zong, and D. M. Ceperley, Phys. Rev. E **64**, 016702 (2001).

[75] J. Trail and R. Needs, J. Chem. Phys. **122**, 014112 (2005).

[76] J. Trail and R. Needs, J. Chem. Phys. **122**, 174109 (2005).

[77] J. R. Trail and R. J. Needs, J. Chem. Phys. **146**, 204107 (2017).

[78] M. P. Nightingale and V. Melik-Alaverdian, Phys. Rev. Lett. **87**, 043401 (2001).

[79] C. J. Umrigar, J. Toulouse, C. Filippi, S. Sorella, and R. G. Hennig, Phys. Rev. Lett. **98**, 110201 (2007).

[80] J. Toulouse and C. J. Umrigar, J. Chem. Phys. **126**, 084102 (2007).

[81] P. R. C. Kent, R. J. Needs, and G. Rajagopal, Phys. Rev. B **59**, 12344 (1999).

[82] N. D. Drummond and R. J. Needs, Phys. Rev. B **72**, 085124 (2005).

[83] M. Snajdr and S. M. Rothstein, J. Chem. Phys. **112**, 4935 (2000).

[84] F. Gálvez, E. Buendıa, and A. Sarsa, J. Chem. Phys. **115**, 1166 (2001).

[85] P. J. Reynolds, D. M. Ceperley, B. J. Alder, and W. A. Lester Jr, J. Chem. Phys. **77**, 5593 (1982).

[86] J. W. Moskowitz, K. Schmidt, M. A. Lee, and M. H. Kalos, J. Chem. Phys. **77**, 349 (1982).

[87] R. Grimm and R. Storer, J. Comp. Phys. **7**, 134 (1971).

[88] E. Hernández, M. J. Gillan, and C. M. Goringe, Phys. Rev. B **55**, 13485 (1997).

[89] D. Alfè and M. J. Gillan, Phys. Rev. B **70**, 161101 (2004).

[90] S. Baroni, P. Giannozzi, and A. Testa, Phys. Rev. Lett. **58**, 1861 (1987).

[91] R. A. Ferrell, Rev. Mod. Phys. **28**, 308 (1956).

[92] L. Dunlop and G. Gribakin, Journal of Physics B: Atomic, Molecular and Optical Physics **39**, 1647 (2006).

[93] P. A. Dirac, in *Mathematical Proceedings of the Cambridge Philosophical Society* (Cambridge University Press, 1930), vol. 26, pp. 361–375.

[94] G. Kontrym-Sznajd and H. Sormann, Phys. Status Solidi B **251**, 140 (2014).

[95] S. Kahana, Phys. Rev. **129**, 1622 (1963).

[96] J. P. Carbotte, Phys. Rev. **155**, 197 (1967).

[97] D. G. Green and G. F. Gribakin, Phys. Rev. Lett. **114**, 093201 (2015).

[98] J. C. Kimball, Phys. Rev. A **7**, 1648 (1973).

[99] M. Matsumoto, M. Tokii, and S. Wakoh, Journal of the Physical Society of Japan **73**, 1870 (2004).

[100] A. Pu, T. Bretagnon, D. Kerr, and S. Dannefaer, Diam. Relat. Mater. **9**, 1450 (2000).

[101] F. Tuomisto, J.-M. Mäki, T. Y. Chemekova, Y. N. Makarov, O. V. Avdeev, E. N. Mokhov, A. S. Segal, M. G. Ramm, S. Davis, G. Huminic, et al., J. Cryst. Growth **310**, 3998 (2008).

[102] J. Mäkinen, P. Hautojärvi, and C. Corbel, J. Phys.: Condens. Matter **4**, 5137 (1992).

[103] H. Weisberg and S. Berko, Phys. Rev. **154**, 249 (1967).

[104] R. Schirhagl, K. Chang, M. Loretz, and C. L. Degen, Annu. Rev. Phys. Chem **65**, 83 (2014).

[105] C. Nguyen, D. Sukachev, M. Bhaskar, B. Machielse, D. Levonian, E. Knall, P. Stroganov, R. Riedinger, H. Park, M. Lončar, et al., Phys. Rev. Lett. **123**, 183602 (2019).

[106] J. Weber, W. Koehl, J. Varley, A. Janotti, B. Buckley, C. Van de Walle, and D. D. Awschalom, Proceedings of the National Academy of Sciences **107**, 8513 (2010).

[107] M. Abobeih, Y. Wang, J. Randall, S. Loenen, C. Bradley, M. Markham, D. Twitchen, B. Terhal, and T. Taminiau, Nature pp. 1–1 (2022).

[108] I. Aharonovich, D. Englund, and M. Toth, Nat. Photon **10**, 631 (2016).

[109] I. Aharonovich, A. D. Greentree, and S. Prawer, Nat. Photon **5**, 397 (2011).

[110] M. Blencowe, Nature **468**, 44 (2010).

[111] J. Wrachtrup and F. Jelezko, J. Phys.: Condens. Matter **18**, S807 (2006).

[112] G. Davies and M. Hamer, Proceedings of the Royal Society of London. A. Mathematical and Physical Sciences **348**, 285 (1976).

[113] L. Rogers, S. Armstrong, M. Sellars, and N. Manson, New J. Phys. **10**, 103024 (2008).

[114] M. L. Goldman, A. Sipahigil, M. W. Doherty, N. Y. Yao, S. D. Bennett, M. Markham, D. J. Twitchen, N. B. Manson, A. Kubanek, and M. D. Lukin, Phys. Rev. Lett. **114**, 145502 (2015).

[115] M. L. Goldman, M. W. Doherty, A. Sipahigil, N. Y. Yao, S. D. Bennett, N. B. Manson, A. Kubanek, and M. D. Lukin, Phys. Rev. B **91**, 165201 (2015).

[116] Y. Ma, M. Rohlfing, and A. Gali, Phys. Rev. B **81**, 041204 (2010).

[117] M. Bockstedte, F. Schütz, T. Garratt, V. Ivády, and A. Gali, Npj Comput. Mater. **3**, 1 (2018).

[118] B. A. Barker and D. A. Strubbe, arXiv preprint arXiv:2207.04549 (2022).

[119] Y. Jin, M. Govoni, and G. Galli, Npj Comput. Mater. **8**, 1 (2022).

[120] A. Gali, E. Janzén, P. Deák, G. Kresse, and E. Kaxiras, Phys. Rev. Lett. **103**, 186404 (2009).

[121] G. Thiering and A. Gali, Phys. Rev. B **96**, 081115 (2017).

[122] A. V. Ivanov, Y. L. Schmerwitz, G. Levi, and H. Jónsson, arXiv preprint arXiv:2303.03838 (2023).

[123] A. J. Cohen, P. Mori-Sánchez, and W. Yang, Science **321**, 792 (2008).

[124] C. A. Coulson and M. J. Kearsley, Proceedings of the Royal Society of London. Series A. Mathematical and Physical Sciences **241**, 433 (1957).

[125] A. Lenef and S. C. Rand, Phys. Rev. B **53**, 13441 (1996).

[126] J. R. Maze, A. Gali, E. Togan, Y. Chu, A. Trifonov, E. Kaxiras, and M. D. Lukin, New J. Phys. **13**, 025025 (2011).

[127] M. Tinkham, *Group Theory and Quantum Mechanics* (McGraw-Hill: New York, 1964).

[128] X. Zhou and F. Wang, Phys. Chem. Chem. Phys. **21**, 20422 (2019).

[129] L. Rao and F. Wang, J. Chem. Phys. **156**, 124308 (2022).

[130] M. Towler, R. Q. Hood, and R. Needs, Phys. Rev. B **62**, 2330 (2000).

[131] W. M. C. Foulkes, R. Q. Hood, and R. J. Needs, Phys. Rev. B **60**, 4558 (1999).

[132] J. Heyd, G. E. Scuseria, and M. Ernzerhof, J. Chem. Phys. **118**, 8207 (2003).

[133] A. Karjalainen, V. Prozheeva, K. Simula, I. Makkonen, V. Callewaert, J. B. Varley, and F. Tuomisto, Phys. Rev. B **102**, 195207 (2020).